Spatial genome reorganization is associated with chromosomal breakage regions and karyotype changes induced by programmed DNA elimination

James R. Simmons[1], Tianchun Xue[2], Rachel Patton McCord[1,2], Jianbin Wang[1,2,3#]

[1] Department of Biochemistry and Cellular and Molecular Biology, University of Tennessee, Knoxville, TN
[2] UT-ORNL Graduate School of Genome Science and Technology, University of Tennessee, Knoxville, TN
[3] Lead Contact

Corresponding author, jianbin.wang@utk.edu

Abstract

Programmed DNA elimination (PDE) is a notable exception to genome integrity, characterized by significant DNA loss during development. In many nematodes, PDE is initiated by DNA double-strand breaks (DSBs), which lead to chromosome fragmentation and subsequent DNA loss. However, the mechanism of nematode DNA breakage remains largely unclear. Interestingly, in the human and pig parasitic nematode *Ascaris*, no conserved motif or sequence structures are present at chromosomal breakage regions (CBRs), suggesting the recognition of CBRs may be sequence-independent. Using Hi-C, we revealed that *Ascaris* CBRs engage in three-dimensional (3D) interactions before PDE, indicating that physical contacts of the break regions may contribute to the PDE process. The 3D interactions are established in both *Ascaris* male and female germlines, demonstrating inherent genome organization associated with the CBRs and to-be-eliminated sequences. In contrast, in the unichromosomal horse parasite *Parascaris univalens*, transient and pairwise interactions between two neighboring CBRs that would form the ends of future somatic chromosomes were observed only during PDE. Intriguingly, we found specific spatial compartmentalization changes in the *Ascaris* chromosomes after PDE converts 24 germline chromosomes into 36 somatic ones. Remarkably, *Parascaris* PDE generates the same set of 36 somatic chromosomes, and the compartment changes following PDE are consistent between the two species. Overall, our findings contribute to a model that the 3D genome facilitates the recognition of sequence-independent break sites for *Ascaris* PDE. It also suggests an evolutionary and developmentally conserved 3D genome reorganization of nematode somatic chromosomes following PDE.

Keywords

Programmed DNA elimination (PDE), DNA double-strand breaks (DSBs), chromosomal breakage regions (CBRs), *Ascaris*, *Parascaris*, nematode, Hi-C, chromosome compartment, karyotype, 3D genome organization.

Introduction

Genome integrity is crucial for faithful inheritance of genetic material. However, during the development of many species, programmed DNA elimination (PDE) removes a substantial portion of the genome, leaving daughter cells with reduced DNA content.[1-6] Although PDE is not found in the common model organisms, it is being discovered in a growing number of species from diverse phyla.[7-14] While PDE is gaining increasing recognition as a significant biological process,[15,16] much remains unknown about its molecular mechanisms, particularly in metazoan species that exhibit PDE.

A major group of PDE species, including most ciliates, many nematodes, and some copepods, use DNA double-strand breaks (DSBs) to fragment the chromosomes before DNA loss.[1,2,6] During their PDE process, specific genomic locations are recognized, DSBs are generated, and DNA break ends are healed. Although the molecular machineries appear to diverge between the ciliates and nematode systems, both sequence-dependent and sequence-independent mechanisms are used for the break site recognition to initiate PDE.[6,7,17] The DSBs in the middle of the germline chromosomes, if healed with telomere addition, can lead to the splitting of the chromosomes and drastic changes in the somatic karyotypes.[18] However, the consequences of the karyotype changes on genome organization and gene expression are largely unexplored.

In the parasitic nematode *Ascaris*, we identified 72 chromosomal breakage regions (CBRs) at the boundaries of retained and eliminated DNA, 48 of which are near both ends of all 24 germline chromosomes.[19] Each CBR contains a 3-6 kb window where new somatic telomere sequences were added to repair the broken ends of DSBs.[19,20] Sequence analysis revealed no significant motifs or sequence structures at these CBRs, suggesting a sequence-independent mechanism for their recognition.[7] Moreover, common histone marks, small RNAs, and R-loops were not associated with the CBRs.[21,22] However, the chromatin at the CBRs is more accessible during PDE, indicating a specific mechanism may be involved.[19,20]

The lack of sequence features associated with *Ascaris* CBRs promotes the search for sequence-independent mechanisms that might be involved in PDE. The eukaryotic genome is organized at a 3D level into folded structures at multiple length scales, involving both intrachromosomal (within the same chromosome) and interchromosomal (among different chromosomes) interactions.[23,24] Changes in 3D genome organization have been implicated in numerous developmental processes, such as V(D)J and class switch recombination in lymphocytes,[25,26] zygotic genome activation during embryogenesis,[27,28] X-chromosome inactivation in mammals,[29,30] dosage compensation in *C. elegans*,[31] antigenic variation and transcription in trypanosomes,[32,33] and neural development.[34,35] We hypothesize that the 3D genome may contribute to PDE by spatially organizing 1) the CBRs before PDE and 2) the resulting somatic chromosomes after PDE. Notably, in *Ascaris*, introducing random exogenous DSBs via X-ray during PDE did not lead to their repair through telomere addition.[36] This further suggests that the DSBs and telomere healing processes associated with *Ascaris* PDE may be confined within specific nuclear compartments and only become functional where the machineries for PDE are concentrated.

Recent advancements in chromosome conformation capture (Hi-C) have unveiled major principles of 3D genome organization, encompassing chromosome territories, compartments, topologically associating domains, and point interactions and acting through mechanisms such as phase separation and loop extrusion. [23,24,37-41] Here, to investigate the association between 3D genome

organization and *Ascaris* PDE, we conducted Hi-C analyses on embryonic stages before, during, and after PDE. We found strong interactions between CBRs before and during PDE, suggesting their potential involvement. These interactions are observed in both male and female germline tissues, implying that intrinsic characteristics of CBRs and eliminated DNA influence the organization of the germline 3D genome. Interestingly, the majority of newly formed somatic chromosomes undergo programmed compartmentalization during embryogenesis, suggesting PDE is crucial to allow the establishment of the new 3D genome organization in the somatic cells. The pattern of *Ascaris* somatic compartments is consistent with that of the horse parasite *Parascaris*, another PDE species with the same somatic chromosomes. This suggests an evolutionarily conserved 3D genome during nematode development. Together, our study provides insights into the dynamics of the 3D genome in nematodes with PDE, shedding light on a possible mechanism for CBR recognition and a potential function of the 3D genome that organizes the somatic chromosomes.

Results

Chromosomal breakage regions interact with each other during *Ascaris* DNA elimination

Ascaris PDE occurs during the 4-16 cell embryonic stages.[7] To explore whether 3D genome organization plays a role in PDE, we performed Hi-C on *Ascaris* embryos at stages before (2-4 cells; 48 hr), during (4-6 cells; 60 hr), and after (32-64 cells; 5 days) PDE. The Hi-C data were mapped to an improved germline genome that corrects previously mis-assembled regions (see Figure S1). Hi-C heatmaps revealed a striking pattern of interactions before and during PDE among chromosome ends where the CBRs reside (Figure 1A, magenta arrows). These interactions are not due to mapping artifacts caused by repetitive sequences, since mapping the Hi-C data to a repeat-masked genome still produced the same pattern of interactions (Figure S2). The interactions also occur among CBRs located in the middle of some chromosomes (Figure 1A, green arrows). The observed/expected Hi-C interactions data further demonstrated the strong interactions of the chromosome ends (Figure 1B). Notably, these interactions disappear after PDE, consistent with the timing of DNA elimination (Figure 1). Overall, the Hi-C data show that genomic regions associated with CBRs exhibit all-against-all interactions. These interactions are specifically associated with the CBRs, and they precede PDE, demonstrating their link to PDE.

CBR interactions are established during germline development

We next asked if the CBR interactions are formed specifically to facilitate PDE. We performed Hi-C on male and female germline tissues and on 1-cell zygotes (0 hr) to determine if the CBRs also interact with each other independent of PDE. These stages were chosen because they are germline stages not associated with PDE. Strikingly, we found that interactions between chromosome ends were already present in both the testes and ovaries, as well as in the 1-cell zygotes (Figure 2). These developmental 3D genome analyses on distinct stages reveal that these long-range CBR interactions are established well before PDE, thus these interactions may be an intrinsic feature associated with the CBRs regardless of developmental stages. Interestingly, the patterns of 3D interactions at the ends of chromosomes exhibited variations among these germline stages (Figure 2). In the testis and 1-cell zygote, the ends of certain chromosomes are observed to interact with the entire length of many other chromosomes, resulting in stripes in the Hi-C maps (Figure 2A and 2C). In contrast, in the ovary, most interactions are more confined to the ends of the chromosomes, as indicated by the dots in the Hi-C maps (Figure 2B). Thus, while our data demonstrate an overall

consistency in the CBR interactions throughout germline development, they also revealed stage-specific variations in the 3D genome interactions.

CBRs are at the boundaries of the spatially organized chromosome ends

To further determine the precise spatial boundaries of the CBR interactions among chromosomes, we mapped *trans*-interaction frequencies (interchromosomal) surrounding the CBRs. Due to the short DNA for many eliminated regions adjacent to CBRs (average 317 kb, median 197 kb), we examined interchromosomal interactions of all CBRs using 100 kb in the eliminated regions and 500 kb in the retained regions (Figure 3A). This analysis revealed a significant enrichment of *trans* interactions within ~200 kb of retained DNA immediately adjacent to the CBRs near the ends of chromosomes (Figure 3A). Strikingly, CBRs reside at the boundaries of the high and low interchromosomal interaction regions (Figure 3A, vertical line), suggesting these strong interactions may spatially demarcate the retained and eliminated sides of the DNA. Interestingly, this spatial separation of retained and eliminated regions is much more prominent for CBRs at the ends of chromosomes than for CBRs in the middle of the chromosomes (Figure S3), indicating that the strong interchromosomal CBR organization is mainly associated with chromosome ends.

The interchromosomal interactions for CBRs are dynamic during embryo development, with the highest interactions observed in the 1-cell embryo; they gradually decrease throughout embryonic development and become minimal by L1 post-PDE (Figure 3A). To further distinguish if the elevated interactions in the CBR-flanking regions were driven by a few selected chromosomes or across all chromosomes, we analyzed the contribution of individual chromosomes (Figure 3B). We found that all chromosomes contributed to the aggregated interactions, suggesting a shared mechanism of 3D genome organization among these chromosomes. Collectively, these results indicate that the chromatin architecture associated with CBRs employs long-range *trans* interactions prior to PDE. These interactions may play a key role in defining the boundaries of 3D genome domains that coincide with the CBRs at the junctions of retained and eliminated DNA.

Short-range interactions and 3D insulation associated with PDE

To explore whether short-range 3D interactions might also influence PDE, we calculated insulation scores across the genome. Insulation scores quantify the degree to which a given region interacts with its local genomic neighborhood. Dips in insulation score can therefore be interpreted as local boundaries across which few interactions occur.[31,42] We identified many regions with dynamic insulation patterns during development (Figure 3C). Notably, out of the 44 completely assembled eliminated regions exceeding 100 kb that allow robust insulation analysis, 35 (80%) consistently exhibited boundary-like dips in insulation score at or near their respective CBRs before the PDE, while six (14%) demonstrated similar drops in insulation score in adjacent retained regions (Figure S4). Conversely, only one eliminated region (chrX5) did not show any sign of boundary-like insulation. These findings suggest that increases in local boundary strength are a common feature of the CBRs associated with PDE.

After PDE, the regions adjacent to CBRs become less insulated as indicated by the increasingly positive insulation scores, extending beyond 1 Mb on either side (Figure 3C). The new chromosome ends also exhibit decreased gene expression, despite showing higher chromatin accessibility measured by ATAC-seq.[20] Consistently, the heterochromatic histone mark H3K9me3 was observed to accumulate at the new chromosome ends after PDE (Figure S5). This decoupling of accessibility

and expression may reflect the repositioning of chromatin domains after PDE liberates the ends of their chromosomes and also splits some germline chromosomes. In contrast, for the non-CBR regions, the insulation is most evident in the eliminated DNA, whereas the retained DNA showed minimal insulation throughout development (Figure 3D). Interestingly, the terminal eliminated regions maintain the highest insulation throughout all stages of embryogenesis, while the internal eliminated regions exhibit greater insulation only in the testis and early embryos through 2-4 cells. The internal eliminated regions become significantly less insulated during the PDE stage (4-8 cells). This difference in insulation between the terminal and internal eliminated regions may be attributed to the fact that internal eliminated regions are flanked by retained DNA on both sides, while the terminal eliminated regions only have one retained neighbor. Overall, these results suggest that the eliminated regions have the least amount of local interactions leading up to PDE, consistent with their higher heterochromatic chromatin content.

Collectively, our data indicate that the CBRs interact with each other before and during PDE. These interactions may play a role in the PDE process by bringing the CBRs to nuclear foci that have accumulated molecular machinery essential for DSBs and telomere addition (PDE foci; see Figure 3E and discussion).

3D chromosomal changes following programmed DSBs for PDE

Following PDE, the 3D genome organization undergoes significant changes. To investigate these changes, we performed Hi-C analysis on staged embryos post-PDE. Initially, we examined the insulation of CBRs (Figure 3C) to determine if the local level interactions had changed after PDE and how the broad insulation varies between the retained and eliminated regions (Figure 3D). Here, to further study the local insulation specific to the CBRs, we determined the insulation scores for 100 kb ends extending into the retained region from both terminal and internal CBRs. We found a consistent pattern of insulation changes (Figure 4A). These CBRs became more insulated from the 1-cell zygote leading up to the time of PDE (4-8 cells) but became more active in local interactions after PDE (32-64 cells) (Figure 4A). This suggests that DSBs may liberate the spatial constraints at the CBRs during PDE, indicating a common response of local genomic contact changes to DSBs at the CBRs. The insulation score of the chromosome ends decreases again in the somatic L1 stage (Figure 4A), likely reflecting the formation of heterochromatin at the new somatic chromosome ends.

Long-range interaction changes and chromosome clustering through PDE

To assess the impact of PDE on intrachromosomal contacts, we analyzed distance decay curves across different stages (Figure 4B). In the 1-cell zygote, interaction frequency exhibits a power-law decay diminishing around 23 Mb, which aligns with the largest germline chromosome sizes. Short-range interactions (<100 kb) increase after PDE, coinciding with the observed increase in local structures seen in the Hi-C heatmap (Figure 1). This suggests the establishment of short-range regulatory interactions throughout the genome. However, mid-range interactions (100 kb to 1 Mb) decline during early embryogenesis through the PDE stage but then rise again post-PDE as somatic chromosomes mature, peaking in L1 larvae. Conversely, long-range interactions (>1 Mb) decrease after PDE, consistent with reduced chromosome sizes. These observations indicate that PDE contributes to the 3D architecture changes by altering both chromosome number and the long-range interactions, ultimately establishing the 3D genome in the somatic nucleus.

To further examine how chromosomes spatially reorganize following PDE, we clustered chromosomes at each developmental stage based on Hi-C contact frequency. In the 1-cell zygote and 2-4-cell embryos, interactions among pre-PDE chromosomes are broadly uniform, with a few chromosome pairs exhibiting stronger-than-average interactions (Figure 4C). After PDE breaks the chromosomes, spatial organization begins to emerge differentially on the somatic chromosomes. A standout feature post PDE is the clustering of sex chromosomes: at 32-64 cells, they form a distinct group separated from the autosomes. This segregation of the sex chromosomes becomes more pronounced in larvae L1. For autosomes, they are organized into several large, distinct clusters, indicating progressive establishment of preferential interactions between chromosome territories (Figure 4C). These data suggest coordinated compartmentalization changes for each chromosome may contribute to the formation of preferred chromosome territory interactions after PDE.

PDE-induced karyotype changes lead to compartmental change and somatic 3D genome reorganization

PDE in *Ascaris* leads to dramatic karyotype changes and the splitting of many germline chromosomes.[19] To investigate whether large-scale chromosomal contact domains change after PDE, we first determined the A/B compartmentalization pattern using the Hi-C data (Figure 5A and Figure S6). Compartmentalization is weak during early development, up to the embryonic stages of PDE (4-16 cells), after which compartments are strengthened (Figure 5A and Figure S7A). This strengthening of compartments likely reflects both large-scale changes in karyotype—due to the increased number of chromosomes following PDE—and smaller-scale chromatin reorganization typical of early embryogenesis in nematodes.[43,44] Overall, our analyses defined *Ascaris* A/B compartments and their changes during early embryo development.

We used a multi-omics approach to validate the compartments inferred from Hi-C (Figure 5B). Data from the 32-64 cell embryos (5 days) were used since they exhibit strong compartmentalization (Figure 5A) and comprehensive multi-omics data are available for this stage. Analysis of strongly compartmentalized regions (defined as EV1 > 0.15 or < -0.15) revealed that active chromatin marks, including H3K4me3, H3S10P, H3K36me2, and H3K36me3, are significantly enriched in A compartments. Conversely, H3K9me3, a marker of repressive chromatin, is significantly enriched in B compartments (Figure 5B). RNA-seq and ATAC-seq analyses also show significantly higher signal in A compartments, corroborating the compartment data. Furthermore, A compartments are enriched for active RNA Polymerase II (Figure 5B). Together, these data confirm that the defined compartments are consistent with the transcriptional activities in the regions.

We observed notable compartmentalization changes surrounding the CBRs before and after PDE. Prior to PDE, the eliminated regions shifted into opposite compartments relative to retained regions. After PDE, chromosomes adopted distinct patterns of A/B compartmentalization (Figure 5). For example, chromosome 1 shows weak compartmentalization between its two future somatic derivatives before PDE with both slightly biased towards the active compartment. Following PDE, the 3' end of chromosome 1a interacts with the 5' end of chromosome 1b within the active compartment, while the 5' end of chromosome 1a and the 3' end of chromosome 1b remain in the inactive compartment (Figure 5A and 5D). A similar pattern is observed for chromosome X1: when X1 is split into three somatic chromosomes, the two terminal fragments occupy the same compartment while the central fragment is segregated away (Figure 5A and 5D). Additional analyses of other somatic chromosomes suggest that compartmentalization changes following PDE are a common feature for all split chromosomes (Figure S6). Interestingly, genome-wide

analysis revealed that in the 32-64-cell embryos, a stage immediately following PDE, the Hi-C compartments exhibit the most variable structure (Figure 5C). This coincides with a significant drop in saddle strength (Figure 5A and Figure S7B), a measure of separation between active and inactive compartments. Compartment identity switching showed a stable pattern before PDE, with similar rates of switching from A-to-B and B-to-B, with most compartments remaining stable (Figure S7C). Immediately after PDE, a significant increase in the ratio of A-to-B switching was observed, while slightly more B-to-A switching was observed between the 32-64 cell and L1 stages. This suggests that the 32-64-cell stage is a transition phase for compartmentalization, where future somatic compartments are yet to be fully established. Notably, however, the split somatic chromosomes undergo specific compartmentalization changes at the L1 stage (Figure 5A and 5D), where the somatic program is fully established. Overall, our findings indicate that PDE-induced karyotype changes contribute to the reorganization of the 3D genome in somatic cells.

CBRs in *Parascaris* form transient and pairwise interactions during PDE

The related horse parasite *Parascaris* undergoes PDE during 2-32 cell embryonic stages.[7,18] *Parascaris* has a single germline chromosome with the majority of the DNA (>85%) in the two heterochromatic arms that will be eliminated. The 72 CBRs are interspersed in the middle of the chromosome where the euchromatic region resides.[18] To determine if the CBRs in *Parascaris* also form 3D genome interactions, we performed Hi-C in embryos before (1 cell; 10 hr), during (2-4 cells; 17 hr), and after PDE (32-50 cells; 36hr). In 1-cell embryos before PDE, the whole chromosome is largely unstructured at the 3D genome level (Figure 6A and Figure S10). However, in 2-4 cells during PDE, we observed a striking pattern of CBR interactions: neighboring pairs of CBRs that will form the ends of future somatic chromosomes interact with each other (Figure 6A-B). When the Hi-C contacts were normalized by the expected pattern of distance decay, 36 sites of higher-than-expected interactions became apparent that match the ends of the 36 future somatic chromosomes (Figure 6B). Like *Ascaris*, these CBR interactions are largely formed in the retained regions (Figure 6C). The enrichment of these pairwise CBR interactions is significantly reduced in 32-50 cells after PDE (Figure 6C). Overall, these data show transient and specific 3D CBR interactions occur only at the time of PDE, suggesting a potential role of the pairwise CBR interactions in *Parascaris* PDE.

Comparative compartment structure in *Parascaris* supports a role for PDE in somatic nuclear reorganization

Previous comparative analyses have shown that *Ascaris* and the closely related parasitic nematode *Parascaris* have the same set of somatic chromosomes after PDE.[18] To determine if programmed compartmentalization changes also occur in *Parascaris*, we performed additional Hi-C on *Parascaris* embryonic stages that match *Ascaris* data. Analysis of the compartments in *Parascaris* showed a strong correlation between the two species throughout the developmental stages (Figure 7). The majority (30/36; 83%) of the correlation coefficients of the eigenvector values are in the range of 0.19-0.95, with the median value at 0.49 (Figure 7). Importantly, for many matching chromosome pairs, such as chr01a/chr05, chr06b/chr07, chr02a/chr16, and chr14/chr21, the compartment patterns seen in *Ascaris* somatic chromosomes after PDE are mirrored in the somatic chromosomes of *Parascaris* (Figure 7). Considering the biological variations of two species that diverged over millions of years[45] and the sampling variations, the similarity of the Hi-C compartments is highly significant. Overall, our result suggests that PDE not only generates the same somatic chromosomes in these two parasites, but the resulting chromosomes undergo the

same programmed compartmental changes after PDE, indicating a conserved feature of the somatic 3D genome for both species after PDE.

Discussion

In the nematode *Ascaris*, the identification of CBRs initiates the PDE processes.[7] However, the mechanism for CBR recognition remains unclear. To investigate this, we used Hi-C to examine the 3D genome organization throughout embryo development. We identified 3D genome interactions among the CBRs associated with PDE and determined the compartmentalization changes in the somatic cells. Our findings revealed that spatial genome organization is not only linked to the CBRs, which may facilitate the PDE process, but it is also conserved between *Ascaris* and *Parascaris* after PDE, which suggests a function of PDE in reorganizing the somatic 3D genomes.

Recognition of CBRs through 3D genome organization.

The Hi-C data revealed that all *Ascaris* CBRs interact with each other during PDE (Figure 1A). These interactions extend beyond the sites of CBRs, often covering the neighboring ~200 kb retained regions (Figure 3). Notably, many CBRs are located at the boundary of the spatially organized chromosome ends (Figure 3). These findings suggest that CBRs are unique to *Ascaris*'s 3D genome organization, as they spatially demarcate the retained and eliminated sides of the DNA. These Hi-C results, combined with previous molecular data, lead us to propose a model for a sequence-independent mechanism of PDE processes in *Ascaris* (Figure 3E). We hypothesize that CBRs interact with each other at sites where machineries for DNA breaks and telomere healing are concentrated (PDE focus; Figure 3E). The model suggests that not all CBRs need to be at the same PDE focus, nor do these interactions need to occur simultaneously. This model matches the population-level Hi-C interactions observed among CBRs during PDE, which are lower than constant interactions but much higher than background-level interactions (Figure 1). The model also aligns with a mechanism that doesn't require nucleotide precision to generate DSBs within the 3-6 kb window, where the broken ends are healed with telomere addition.[36]

A plausible mechanism for organizing the PDE foci is through phase-separated condensates.[38,46-49] In other systems, such as olfactory receptor clustering in mammalian cells, phase-separated condensates can reinforce strong interchromosomal interactions similar to the ones observed between CBRs.[50] We suggest proteins and RNAs involved in DNA breaks and telomere addition may accumulate during PDE to facilitate the formation of PDE foci. For instance, during *Ascaris* PDE, DSB ends are resected to generate long single-strand DNA (ssDNA) overhangs for telomere addition.[36] The ssDNA likely binds to PRA, a protein known for its strong propensity to form dynamic condensates.[51] This model is consistent with exogenous DSBs not localizing to PDE foci and not healed with telomeres.[36] In addition, existing germline telomeres and shelterin components could also contribute to the formation of liquid-like droplets.[52,53] This may explain why CBRs at the boundaries of spatially organized 3D domains are mostly observed at the ends of germline chromosomes where telomeres are present (Figure 3 and Figure S3). Furthermore, the co-localization of chromatin regions at sites enriched for processing enzymes is precedented by phenomena such as RNA splicing speckles.[54] Additional factors, such as sequence- or nucleosome-dependent elements, may further contribute to the positioning of the CBRs for DSB generation. Overall, our data suggest that CBRs represent a unique genomic feature in nematodes with PDE, and the 3D genome organization of the CBRs and chromosome ends may contribute to their recognition to initiate and/or execute PDE. Future experiments are necessary to 1) localize the

CBRs in the nucleus, 2) identify proteins that interact with CBRs, and 3) determine the machineries involved in DNA break, end processing, and telomere healing.

The CBR and chromosome end interactions are also observed in the germline and early embryos before PDE (Figure 2). While it remains to be determined if these interactions persist through fertilization and pronuclear fusion or if they are erased and re-established in the zygote, these interactions in germline stages suggest they may not be specifically formed for PDE. Instead, these interactions may serve a germline function, likely involved in meiosis. In *C. elegans*, pairing and synapsis are achieved through the recognition of the pairing centers at one end of each chromosome by four related zinc finger proteins.[55,56] Interestingly, these zinc finger protein genes and many other genes involved in *C. elegans* pairing are absent in *Ascaris* and *Parascaris*,[18] suggesting that nematodes with PDE may use different mechanisms for pairing. Our data provide support that indeed, these germline chromosomes can interact with each other using their chromosome ends (Figure 2). These interactions may be an intrinsic feature associated with the sequences at the chromosome ends. During PDE, these sequences, along with their 3D interactions, are removed. Therefore, PDE may offer a means to remove chromosome ends that function in germline pairing but are no longer required or may even be harmful in somatic cells.

The CBRs from *Parascaris* also interact during PDE. However, unlike *Ascaris* CBRs that form all-against-all interactions, *Parascaris* CBRs engage in pairwise interactions only for CBR pairs from the future ends of each somatic chromosome. The *Parascaris* pairwise CBR interactions are weaker than *Ascaris* CBR interactions and occur transitionally only during PDE stages. They are reminiscent of the "beads-on-a-string" model based on an early cytology study,[57] where the "beads" are the retained and condensed future somatic chromosomes, and the "string" is the eliminated and more loose chromatin during PDE. Thus, our Hi-C data corroborate the cytologic observation that the CBRs in *Parascaris* are at the boundaries of spatially organized chromosomes that could separate the retained and eliminated DNA at the 3D level (Figure 4). The differences in CBR interactions observed in these two nematodes suggest possible variations in the PDE mechanisms, some of which may be attributed to the unique organization of the single pair of *Parascaris* germline chromosomes, where none of the CBRs are at the ends of the chromosomes.[18]

PDE provides a means to reorganize the somatic chromosomes.

Ascaris and *Parascaris* split evolutionary fused germline chromosomes into the same set of 36 somatic chromosomes.[18] We previously suggested that the restoration of the somatic karyotype may confer biological functions.[18] Here, we demonstrate that the 3D genome organization, as exemplified by the compartmentalization changes following PDE, is conserved between the two species (Figure 7). While the impact of these compartmentalization changes on individual genes may be limited or negligible, the aggregate effect from numerous genes influenced by these changes could be substantial. Although the evolutionary trajectories leading to the current germline chromosomes appear to differ,[18] the somatic chromosomes have retained the "memory" of 3D genome organizations after PDE. This underscores the important role of PDE in splitting the fused germline chromosomes.

Chromosome reorganization is a common response to DSBs.[58-61] Unlike most DSBs that are repaired using non-homologous end joining or homologous recombination, DSBs induced by PDE in *Ascaris* are healed through telomere addition, accompanied by DNA loss.[36,62] This telomere-mediated repair process may also contribute to chromosome reorganization by forming

condensates surrounding the CBRs. Interestingly, analysis of the Hi-C data across all 36 somatic chromosomes throughout the PDE stages revealed consistent temporal changes in the 3D genome structure of DSBs. These changes were observed in the decreased insulation following PDE (Figure 4A). This change may be attributed to the liberation of CBRs from their germline chromosome locations, the DSB and telomere healing mechanisms, and the formation of new somatic heterochromatins at the chromosome ends. Future analysis of the impact of DSBs in genetically tractable nematodes is promising to provide novel insights into the phenotypic and molecular consequences associated with DSBs.

In *C. elegans* and other rhabditid nematodes, Hi-C compartments are also observed.[31,63-66] These compartments exhibit a general profile for autosomes, where the active (A) compartment is in the middle of the chromosomes and inactive (B) compartments are in the arms of the chromosomes, forming a linear B-A-B profile along its arm-center-arm.[67] This B-A-B profile is consistent with expression data that more conserved and active genes are located in the middle of the chromosomes.[68] Comparative analysis indicates that this compartmental organization may be associated with the ancestral linkage groups in nematodes (known as Nigon elements[69,70]), as fused chromosomes retain the centrality of the active compartment.[71] Interestingly, this compartment profile is not consistently observed in *Ascaris* and *Parascaris* somatic chromosomes, despite that Nigon elements are largely maintained in their genomes.[18] Some of these differences could be attributed to the more discrete early embryo stages used in our study, although Hi-C data from a strictly somatic tissue (such as the intestine) also did not exhibit a consistent compartment profile.[18] Since *Ascaris* and *Parascaris* belong to the distant clade III of nematodes, it is plausible that their compartment profiles may have diverged from those of rhabditid nematodes (clade V). Thus, additional Hi-C data on more nematodes is necessary to further elucidate the commonalities and variations in compartment formation and 3D genome dynamics during development.

3D genome organization and its association with other PDE species.

In the free-living nematode *Oscheius tipulae*, the recognition of break sites is facilitated by a conserved motif known as the Sequence for Elimination (SFE). This motif marks break sites near the ends of all germline chromosomes.[72] Genetic analysis has shown that the SFE is both necessary and sufficient for the process of PDE, as insertion of the SFE in various regions of the genome can trigger PDE (Dockendorff, personal communication). However, this does not necessarily imply that 3D genome organization did not play a role in facilitating PDE. More functional studies are needed to determine the contribution of the 3D genome to the organization of the SFEs for *O. tipulae* PDE.

A recent study in the ciliate *Oxytricha trifallax* suggested widespread 3D genome reorganization before the onset of PDE.[73] Hi-C data on sorted nuclei from developmental stages before and after PDE indicate that the 3D genome reorganization differentiates retained DNA from eliminated regions. This finding is consistent with our observation that CBRs spatially demarcate retained and eliminated DNA in nematodes (Figure 3). Ciliates are a diverse group that exhibits considerable variations in the mechanisms involved in PDE.[13,74,75] It would be intriguing to investigate whether 3D genome changes can also be linked to other ciliates that undergo PDE.

Conclusions

PDE is an exception to the genome constancy rule. The mechanisms of PDE, particularly in multicellular organisms, remain largely unknown. The association of DNA break sites with 3D genome organization presents opportunities for studying the mechanisms of DSBs. PDE, as an integral part of development in many organisms, creates drastic karyotype changes, often leading to the splitting of chromosomes. These PDE organisms offer excellent platforms to investigate the impact of 3D genome reorganization caused by PDE-induced karyotype changes. As the number of known PDE species increases, further studies are crucial to unravel the function of the 3D genome in the mechanisms and consequences of PDE.

Acknowledgments

We thank Martin Neilsen for the *Parascaris* material and Bruce Bamber, Jeff Myers, and Routh Packing Co. for their support and hospitality in collecting *Ascaris* material. We also thank the Wang lab members for helpful discussions and Dick Davis for comments and critical reading of the manuscript. This work was supported by NIH grants to J. W. (AI155588 and GM151551) and the University of Tennessee Knoxville Startup Funds.

Author contributions

J.R.S. and J.W. designed the project; J.R.S. made Hi-C libraries; J.R.S. improved the *Ascaris* genome assembly; J.R.S., T.X., and R.P.M. performed Hi-C data analysis; J.R.S. wrote the initial draft; J.W. wrote the manuscript; J.R.S., R.P.M., and J.W. reviewed and edited the manuscript; J.W. and R.P.M. provided supervision; and J.W. managed the project and provided funding.

Declaration of interests

The authors declare no competing interests.

Figure legends

Figure 1. CBRs interact with each other during *Ascaris* PDE. A. Hi-C heatmaps on *Ascaris* embryos from developmental stages before (2-4 cells, 48 hours), during (4-8 cells, 60 hours), and after (32-64 cells, 5 days) PDE. Hi-C interactions are observed between the ends of chromosomes where CBRs reside before and during PDE. Notably, these interactions are not observed after PDE at the 32-64 cell stage. Values were normalized using counts per million (CPM). Magenta arrows indicate two instances of interactions at the ends of the chromosomes, while green arrows denote two examples of interactions at the middle of the chromosomes. **B.** Observed/expected transformed Hi-C data from **A**, highlighting the interactions among the ends of chromosomes. These interactions are depleted after PDE in the 32-64-cell embryos.

Figure 2. CBR interactions are established during germline development. Interactions between chromosome ends were present in the testis (**A**), ovary (**B**), and 1-cell zygote (**C**). Values were normalized using counts per million (CPM). Note the differences in the dots (Ovary) vs. stripes (Testis and 1-cell zygote) for the interactions.

Figure 3. Interactions of CBR-adjacent regions are associated with PDE. A. CBR-adjacent regions have high interchromosomal interactions. The CBRs are highlighted in green with a vertical dashed line and designated as 0. The 500-kb retained side is to the left, and the 100-kb eliminated side is to the right. *Trans* interaction frequencies surrounding the CBRs at the ends of chromosomes are shown. Interactions among chromosomes were aggregated for each CBR-adjacent region using a 5-kb bin size. Meta-profiles for all analyzed CBRs are displayed as mean (solid lines) ± one standard error of the mean (SEM, shaded areas). **B.** All chromosomes are contributing to the CBR interactions observed in **Figure 3A**. The aggregated CBR *trans*-interaction for the testis was broken down by contributions from each chromosome (ordered and color-coded). **C.** CBR regions are highly insulated in the germline and early embryos through PDE. Insulation score is shown for each developmental stage for chromosome 2. Less insulated regions (positive values) are shown in blue (above), more insulated regions (negative values) are shown in red (below). Eliminated regions are highlighted in red. c = cell(s). **D.** The end eliminated regions are highly insulated. The whole genome is broken down by retained (blue), end eliminated (red), and internal eliminated (orange) regions. Insulation score values using a 100-kb window size are plotted for each developmental stage in a sliding window size of 5 kb. Post-PDE stages on the right are highlighted in red. **E.** Interaction of CBRs at PDE foci in the nucleus. A 3D genome interaction model based on Hi-C maps. Shown are the dynamic changes of the CBRs (red circles) in five chromosomes (five colored threads in their chromosome territories). PDE foci are shown in big yellow circles. Germline (old; green) and somatic (new; blue) telomeres are in small green and dark green circles, respectively. Depicted are two CBRs interacting within a PDE focus (left, top), where a DSB occurred. After DSB formation, new telomeres are added to the retained DNA, which then dissociates from the PDE foci (right, top). A newly formed CBR interaction is also shown (right, bottom).

Figure 4. 3D chromosomal changes during embryogenesis or in response to programmed DSBs. A. Dynamic changes of insulation for retained ends of chromosomes. Insulation scores for 100 kb regions of retained DNA proximal to the end (47 sites; left) and middle (24 sites; right) of the chromosomes were determined using Hi-C contact matrices at 20-kb resolution with a 100-kb insulation square size. Shown are means with bars representing one standard error. Each dot represents the end of a somatic chromosome (or future somatic chromosome in pre-PDE stages).

B. Changes in middle and long-range Hi-C interaction. Distance-decay curves for whole-genome Hi-C interaction data at different developmental stages. Normalized expected contact frequency (y-axis) is plotted against genomic distance (x-axis) on a log-log scale. **C.** Changes in the 3D interaction among chromosomes. Chromosomal cluster analysis was performed at each developmental stage. Pre-PDE genomes are shown with 24 chromosomes, while post-PDE genomes are shown with 36 chromosomes. Strong clusters emerge after PDE as seen in the group of sex chromosomes in the top-left corner (in 32-64 cell and L1).

Figure 5. PDE splits chromosomes and causes 3D genome changes. A. Compartmentalization changes during *Ascaris* embryogenesis. Hi-C compartments were determined by using the Eigenvector 1 values of chromosomes through the developmental stage. Eliminated regions are highlighted in red (see Figure S4 for compartments for all chromosomes). **B.** Multiomics analysis confirms the defined compartments. Markers of active chromatin are enriched in A compartments, while a marker of heterochromatin is enriched in B compartments. Each point represents a 100 kb genomic region. A Mann-Whitney U test was performed to calculate the statistical significance. **C.** Dynamics of compartment interactions through development. A/B compartment interactions are shown using saddle plots, which show interaction frequencies as a function of compartment identity and magnitude, representing the spatial separation of active and inactive chromatin domains. Genomic bins are sorted by PC1 value and binned into 20 quantiles (both axes). Contact enrichment within each bin pair is displayed (red = high; blue = low). Dashed lines mark the A/B boundary (PC1 = 0). **D**. Model of chromosomal rearrangements following PDE. The germline chromosomes are not strongly compartmentalized in the early embryos. After PDE, the resulting somatic chromosomes reorganize their compartments. For autosome chr1, the right end of chr1a interacts with the left end of chr1b within the active compartment, while the remaining regions are positioned in the inactive compartment. For sex chromosome X1, which is broken into three somatic chromosomes, the chrX1a and chrX1c are in the same compartment, while chrX1b is separated into a different compartment.

Figure 6. Transient end-to-end cis interactions between *Parascaris* CBRs during PDE. A. Hi-C contact map of the *Parascaris* embryos before and during PDE. The interaction between the boundaries of the sex chromosome region (yellow box) is due to the 25% of the Y chromosome in the population of embryos that lack the sex chromosome region (karyotype: female = XX and male = XY).[18] **B.** Pairwise CBR interactions during *Parascaris* PDE. Observed/expected contact ratio map for the same stages as in **Figure 6A**. Strong focal interactions are visible between the two CBRs that define the ends of each future somatic chromosome. **C.** Transient CBR interactions through *Parascaris* embryogenesis. Developmental Hi-C maps show that these end-to-end CBR interactions are not present in early embryos or prominent in late embryos. They peak at the 2-4 cell stage, where PDE occurs.

Figure 7. Chromosomal compartments are conserved between *Ascaris* and *Parascaris*. Eigenvector 1 values show conserved compartmentalization between *Ascaris* (red) and *Parascaris* (blue) after PDE. Positive values represent A (active) compartments and negative values represent B (inactive) compartments. Eliminated regions are shown with red highlights. The chromosomes are ordered based on their position along the length of the single germline chromosome of *Parascaris*, with the coordinates shown at the bottom in Mb. Matching somatic chromosomes in *Ascaris* that are flipped on the x-axis (i.e., genome coordinates) are labeled with (R).

Materials and Methods

Nematode Sample Collection and Staging. *Ascaris* ovaries and testes were dissected from adult worms. *Ascaris* 1-cell embryos were collected from fresh ovaries by dissolving the tissue with two treatments: 0.5 N NaOH for 60 min at room temperature, followed by washing in cold PBS buffer, pH 2.0. Embryonation of *Ascaris* zygotes was performed in PBS, pH 2.0, at 30°C while shaking for 10 hr (1 cell), 48 hr (2-4 cells), 60 hr (4-8 cells), 5 days (32-64 cells), and 10 days (L1 larvae). Ovary, testes, and staged embryos were frozen in liquid nitrogen and stored at -80°C until use.

Collection of *P. univalens* zygotes and embryonation were performed as previously described.[18] Dissected zygotes were stored at 4°C. Embryonation was performed in PBS, pH 2.0, at 37°C while shaking for 0 hr (1 cell), 17 hr (2-4 cells), 24 hr (4-8 cells), 48 hr (100-500 cells), 60 hr (300-800 cells), or 72 hr (L1 larvae).

Decoating of *Ascaris* and *Parascaris* embryos was performed by resuspending embryos in 0.4 N KOH/1.4% sodium hypochlorite and incubating for 90 min at 30°C, shaking at 100 RPM. Embryos were washed in cold PBS, pH=7.0, five times and pelleted at 1250 x g for 5 min to estimate the volume of decoated embryos. Staging and decoating of *Ascaris* and *Parascaris* embryos were confirmed by visual inspection under a compound light microscope at 40X magnification.

Hi-C Library Preparation. Fixation was performed using the standard input protocol for *Ascaris* ovaries and testis. For both *Ascaris* and *Parascaris* embryos, the low input protocol was used, with the following modification: cell membranes were disrupted by forcing cells through a small metal dounce in 5 mL of PBS + TC buffer (fixative solution) kept on ice. Hi-C was performed using the Arima-HiC 2.0 kit according to the manufacturer's protocol (Arima, Cat#A410110). After cross-linking and digestion, samples were fragmented using the Covaris M220 ultrasonicator (Covaris, Cat#500295) with the following settings: temperature = 7°C, peak incident power = 75 W, duty factor = 5%, cycles per burst = 200, time = 70 s. This yielded fragments of around 500 bp. Size selection was performed using AMPure XP magnetic beads (Beckman Coulter, A63881). Illumina libraries were constructed using the Swift Biosciences Accel-NGS 2S Plus DNA Library kit (Swift Cat# 21024) and the NEBNext Ultra II DNA Library Prep Kit (NEB). Libraries were amplified using the KAPA Library Amplification kit (Roche Cat# KK2620) according to the manufacturer's protocols. Sample concentrations were measured with a DNA Qubit (Invitrogen, Cat# Q33238), and library fragment sizes were confirmed using a TapeStation 4200 (Agilent). Illumina libraries at 150 bp were sequenced using a NovaSeq 6000 at the University of Colorado Anschutz Medical Campus Genomics Core to a depth of 16-60X.

Multi-omics Data Generation. The following datasets used for multi-omics analysis were previously published: ATAC-seq, RNA-seq, ChIP-seq for histone marks (H3K4me3, H3S10P, H3K36me2, H3K36me3, H3K9me3), and RNA Polymerase II.[19,20,76,77]

Computational Analysis

***Ascaris* Genome Assembly and Improvement.** The germline *Ascaris* genome assembly was systematically refined through iterative manual curation guided by Hi-C contact maps. Initial improvements included correcting obvious mis-assemblies, filtering unplaced scaffolds, and repositioning genomic segments based on artifactual Hi-C interaction patterns. Throughout this process, Hi-C contact heatmaps were generated at multiple resolutions to visually identify mis-

assemblies. Corrections were implemented iteratively until contact maps displayed canonical chromatin interaction patterns with minimal obvious structural artifacts. Previously unplaced contigs were integrated into chromosomes where Hi-C linkage data supported their placement. The assembly was further improved by breaking the genome at scaffold junctions and re-scaffolding using Hi-C proximity ligation data. Chromosome termini were extended toward telomeres by mapping PacBio long reads to the corrected assembly, filtering previously incorporated reads, and using unmapped telomere-containing reads and contigs to extend chromosome ends. CBR coordinates from the previous *Ascaris* assembly were transferred to the updated genome using BLAST[78] to define both terminal and internal CBR sites in the updated assembly.

Hi-C Data Processing. Paired-end Hi-C reads were aligned to the *Ascaris* reference genome using Bowtie2,[79] and contact matrices were generated with HiC-Pro.[80] AllValidPairs files were converted to .hic format using hicpro2juicebox from HiC-Pro for downstream analysis. Standard HiC-Pro quality control metrics were computed for all samples, including mapping rates, valid interaction percentages, and trans/cis interaction ratios. Repetitive sequences were not masked in the primary analysis; a control analysis with repeat masking was performed separately to assess the impact of repeat filtering (Figure S2). For contact map visualization, allValidPairs files were converted to .cool/.mcool format. Heatmaps were generated at 250 kb resolution using raw contact counts normalized to counts per million (CPM): CPM = (raw counts / total valid pairs) × 10^6. Downstream analyses used both .hic files and HiC-Pro-generated contact matrices at appropriate resolutions for each application.

Trans-Chromosomal Interaction Analysis at CBRs. Trans-chromosomal Hi-C interactions were quantified from allValidPairs files for pre- and post-elimination developmental stages. The genome was partitioned into 5 kb bins, and trans interaction counts (interactions between different chromosomes) were aggregated for each bin. Counts were normalized to counts per million (CPM) mapped reads. For each CBR, interaction profiles were computed by extracting bins within 500 kb windows upstream (into the retained region) to 100 kb downstream (into the eliminated region) around the CBR midpoint. Individual CBR profiles were aggregated across either all end CBRs or across all internal CBRs to generate meta-profiles for each developmental stage. To quantify which chromosomes contributed to the elevated trans interactions near the CBRs, partner chromosome contributions were represented proportionally based on normalized interaction frequencies.

Insulation Score Analysis. Chromatin insulation scores (where lower values indicate stronger insulation and higher values indicate weaker insulation) were calculated from Hi-C contact matrices at 20 kb resolution using a 100 kb insulation square size and 80 kb insulation delta span. To visualize insulation dynamics across programmed DNA elimination, insulation scores from pre-elimination samples were plotted directly on germline genome coordinates, while post-elimination samples were mapped back to pre-elimination coordinates using syntenic region mappings. Eliminated regions were highlighted but excluded from post-elimination plots to avoid artifacts. For genome-wide visualization, insulation scores were plotted for all chromosomes at each developmental stage (1 cell, 2-4 cell, 4-8 cell, 32-64 cell, L1 larva). Smoothing was applied using a moving average filter (10 bin window).

Multi-Omics Analysis of New Somatic Chromosome Ends. To characterize the chromatin state at newly formed somatic chromosome ends following DNA elimination, we defined 100 kb terminal regions reaching from each CBR into the neighboring retained region. CBRs were separated for analysis by their presence at the end of chromosomes or internally/near the middle of a

chromosome. For each developmental time point, multiple genomic and epigenomic datasets were analyzed as available: insulation scores (chromatin domain organization), RNA-seq (gene expression at 50 kb resolution), ATAC-seq (chromatin accessibility at 50 kb resolution), H3K9me3 ChIP-seq (heterochromatin mark at 50 kb resolution), and H3K4me3 ChIP-seq (active chromatin mark at 50 kb resolution).

For each 100 kb end or middle region, mean values were calculated by averaging all bins that overlapped the region. When multiple biological replicates were available (ATAC-seq, ChIP-seq), values were first averaged across replicates before regional quantification. Data were visualized across five developmental stages spanning pre-elimination (1 cell, 2-4 cell, 4-8 cell) through post-elimination (32-64 cell, L1 larva) timepoints. Statistical comparisons between each time point were performed using two-sided Mann-Whitney U tests. Data were plotted as mean ± one standard error of the mean (SEM), with individual data points representing a single chromosome end. Sample sizes (n) represent the number of chromosomal regions analyzed at each time point.

A/B Compartment Analysis. To determine the compartments, we use Principal Component Analysis (PCA) on the normalized Hi-C contact matrix to identify the leading eigenvector. This primary PC is often reliable in identifying the A/B compartments.[81] However, for the *Parascaris* Hi-C analysis, the A and B compartments may need to be swapped in certain cases based on additional genomic data, such as histone markers, RNA-seq, and RNA pol II ChIP-seq (Figure S6). Additionally, in early embryos, the first PC may not accurately represent the A/B compartments due to limited distinct Hi-C interactions, among other factors. In such cases, we manually examine these instances and adjust the compartment call when necessary (Figure S6).

Validation of Compartment Identity with Multi-Omics Data. To validate the biological accuracy of A/B compartment assignments, we integrated genomic and epigenomic datasets at the 32-64 cell stage. This stage was chosen as it represented the most complete dataset and showed strong compartmentalization. Eigenvector values (100 kb resolution) were matched with multiple 10 kb resolution datasets, including RNA-seq, PRO-seq, ATAC-seq, and ChIP-seq for histone modifications (H3K4me3, H3K27me3, H3K9me3, H3K36me3, H3K36me2, H3K27me1, H4K20me1, H3S10p, H2AK119ub), RNA Polymerase II, and centromeric proteins (CENP-A, CENP-C). For each 100 kb eigenvector bin, overlapping 10 kb omics bins were identified, and signal values were averaged to match resolutions. Bins were classified as A compartment (eigenvector > 0) or B compartment (eigenvector < 0). Statistical significance of signal differences between A and B compartments was assessed using two-sided Mann-Whitney U tests.

Compartment Strength Analysis. A/B compartment interactions were analyzed using saddle plots, which aggregate Hi-C contact frequencies as a function of compartment identity. For each developmental stage, 100 kb resolution contact matrices and eigenvector (PC1) values were used. Genomic bins were sorted by PC1 value and partitioned into 20 quantiles to ensure even distribution. Contact frequencies between all bin pairs were then aggregated according to their quantile assignments, creating a 20×20 saddle matrix. Saddle strength was quantified as the ratio of within-compartment to between-compartment interactions: (AA + BB) / (AB + BA), where AA represents mean contact enrichment between A compartment bins, BB between B compartment bins, and AB between A and B compartment bins. This measures compartment segregation, with higher values indicating stronger separation between euchromatic (A) and heterochromatic (B) compartments. Compartment strength was calculated as the mean absolute PC1 value. Compartment switching between consecutive developmental stages was assessed by comparing

PC1 signs for each genomic bin. Bins were classified as stable (maintaining A or B identity), A-to-B switches, or B-to-A switches. Only bins with |PC1| > 0.005 were included in the switching analysis to exclude weakly defined compartments. Statistical significance of switching frequencies was evaluated using two-sided Mann-Whitney U tests.

Expected Contact Frequency Analysis. Expected Hi-C contact frequencies as a function of genomic distance were computed from .hic files using FAN-C.[82] For each sample, genome-wide expected contact matrices were generated at 100 kb resolution. Genome-wide expected contact profiles were combined across all samples by aligning contacts at equivalent genomic distances. Plots were normalized by scaling each sample's profile such that the contact frequency at the first distance bin equaled the average across all samples at that distance, allowing direct comparison of decay rates independent of absolute interaction counts.

Chromosome Interaction Clustering Analysis. Whole-chromosome trans interaction patterns were analyzed to identify chromosomes with similar interaction profiles before and after programmed DNA elimination. Inter-chromosomal interactions were extracted from allValidPairs files for pre-elimination samples (24 intact chromosomes) and post-elimination samples (36 chromosomal segments following DNA elimination). Mitochondrial and unplaced scaffolds were excluded from analysis.

For each sample, raw interaction counts between chromosome pairs were compiled into symmetric interaction matrices by averaging reciprocal interactions (i.e., interactions from chromosome A to B and B to A). Self-interactions were excluded (set to NaN). Matrices were normalized using an expected-trans interaction model where expected interaction frequencies between chromosome pairs were calculated based on the total trans interaction counts for each chromosome. Normalized values were computed as observed/expected ratios. Interaction matrices were visualized as clustered heatmaps with hierarchical dendrograms displayed along both axes to illustrate chromosome relationships.

Comparative Compartment Analysis Between Species. A/B compartment structure was determined for *Ascaris* and *Parascaris* from Hi-C data using principal component analysis (PCA) on normalized contact matrices at 100 kb resolution, implemented in FAN-C. The first eigenvector (EV1) of the observed/expected contact matrix was computed genome-wide and oriented by correlation with GC content, where positive values indicate GC-rich, open A compartments and negative values indicate GC-poor, closed B compartments. Post-elimination *Parascaris* chromosomal segments were mapped back to pre-elimination germline coordinates to establish a common reference frame. *Ascaris* chromosomes were similarly mapped to *Parascaris* homologs using chromosome-level synteny,[18] with coordinates scaled proportionally to account for length differences between species.

For each species, EV1 profiles were corrected for arbitrary sign by applying chromosome-specific polarity adjustments to ensure biological consistency across homologous regions. Profiles were smoothed using a rolling mean (window size = 3 bins) to reduce noise while preserving large-scale compartment structure. Eliminated regions were highlighted but excluded from quantitative analysis. The degree of compartment conservation between homologous chromosomes was quantified using Pearson correlation coefficients. For each chromosome pair, EV1 values from *Ascaris* and *Parascaris* were interpolated to 100 common genomic positions spanning the

homologous region, and correlation was calculated after applying appropriate coordinate transformations (i.e., reversals for inverted syntenic blocks).

Artificial Intelligence Usage. Hi-C data processing and visualization were performed with custom Python and shell scripts. Script development and debugging were assisted by Claude Sonnet 4.1 and 4.5 (Anthropic), with all outputs verified through manual inspection and comparison with published methods. Claude was used to refine some manuscript text for clarity and conciseness.

Data availability

The Hi-C data will be deposited in the NCBI GEO database.

Supplemental figure legends:

Figure S1. Hi-C contact maps demonstrate improved genome assembly quality. 2-4 cell stage data mapped to the previous *Ascaris* assembly (left) and updated assembly (right) for representative chromosomes.

Figure S2. Effect of repeat masking stringency on *Ascaris* 2-4 cell Hi-C contact maps. Unscreened: no repeat masking. Screened 10-1: genomes masked at increasing stringency thresholds, where tandem repeats present the listed numbers of times are progressively masked. Chromosomes are labeled by name.

Figure S3. Trans-chromosomal interaction frequencies flanking internal chromosomal break regions (CBRs, green) across *Ascaris* developmental stages. Interactions among chromosomes were aggregated for each CBR-adjacent region using a 5-kb bin size. Meta-profiles for all analyzed CBRs are displayed as mean (solid lines) ± one standard error of the mean (SEM, shaded areas).

Figure S4. Insulation score profiles across *Ascaris* chromosomes at five developmental stages. Red shading indicates eliminated regions. Autosomes (blue) and sex chromosomes (magenta) are shown with genomic coordinates below in Mb. Chromosomes are labeled with their germline names at the bottom and their somatic names (when applicable) at the top of each plot. The data was smoothed across a 10-bin window for clarity.

Figure S5. Chromatin state dynamics at somatic chromosome termini. Multi-omics analysis of 100 kb terminal regions flanking programmed DNA elimination breakpoints in *Ascaris*, including ATAC-seq, RNA-seq, and H3K9me3 ChIP-seq. The values shown are means with bars representing one standard error. Each dot represents the end of a somatic chromosome (or future somatic chromosome in pre-PDE stages). New chromosomal ends near end CBRs are shown on the left of each plot, while new ends that form from internal breaks are on the right.

Figure S6. Compartment eigenvector (PC1) profiles across *Ascaris* chromosomes at five developmental stages. Red shading indicates eliminated regions. Autosomes (blue) and sex chromosomes (magenta) are shown with genomic coordinates below in Mb. Chromosomes are labeled with their germline names at the bottom and their somatic names (when applicable) at the top of each plot. The data was smoothed across a 3-bin window for clarity.

Figure S7. Genome-wide compartmentalization dynamics during *Ascaris* embryogenesis. **A.** Compartment strength (mean |PC1| in 100 kb bins) across developmental stages. **B.** Saddle plot quantification showing A-A, A-B, and B-B interaction enrichments and combined strength metric (AA+BB)/(AB+BA) for each stage. **C.** Compartment switching between consecutive stages: scatterplots (left), frequency distribution (center), and magnitude histograms (right). In the scatterplots, grey dots represent bins that did not change A/B identity between stages, while red dots represent bins that did change A/B identity. In the frequency distribution and histograms, blue represents A-to-B switching, while red represents B-to-A switching.

Figure S8. Hi-C contact map of *Parascaris univalens* 10-hour embryo. A gold bar denotes the sex chromosome region absent from the male Y chromosome. Genome coordinates are shown on both axes in Mb.

References

1. Wang, J., and Davis, R.E. (2014). Programmed DNA elimination in multicellular organisms. Curr Opin Genet Dev *27C*, 26-34. 10.1016/j.gde.2014.03.012.
2. Zagoskin, M.V., and Wang, J. (2021). Programmed DNA elimination: silencing genes and repetitive sequences in somatic cells. Biochem Soc Trans *49*, 1891-1903. 10.1042/BST20190951.
3. Dedukh, D., and Krasikova, A. (2021). Delete and survive: strategies of programmed genetic material elimination in eukaryotes. Biol Rev Camb Philos Soc. 10.1111/brv.12796.
4. Drotos, K.H.I., Zagoskin, M.V., Kess, T., Gregory, T.R., and Wyngaard, G.A. (2022). Throwing away DNA: programmed downsizing in somatic nuclei. Trends Genet *38*, 483-500. 10.1016/j.tig.2022.02.003.
5. Kloc, M., Kubiak, J.Z., and Ghobrial, R.M. (2022). Natural genetic engineering: A programmed chromosome/DNA elimination. Dev Biol *486*, 15-25. 10.1016/j.ydbio.2022.03.008.
6. Mochizuki, K. (2024). Programmed DNA elimination. Curr Biol *34*, R843-R847. 10.1016/j.cub.2024.07.103.
7. Estrem, B., and Wang, J. (2023). Programmed DNA elimination in the parasitic nematode Ascaris. PLoS Pathog *19*, e1011087. 10.1371/journal.ppat.1011087.
8. Streit, A., Wang, J., Kang, Y., and Davis, R.E. (2016). Gene silencing and sex determination by programmed DNA elimination in parasitic nematodes. Curr Opin Microbiol *32*, 120-127. 10.1016/j.mib.2016.05.012.
9. Smith, J.J., Timoshevskiy, V.A., and Saraceno, C. (2021). Programmed DNA Elimination in Vertebrates. Annu Rev Anim Biosci *9*, 173-201. 10.1146/annurev-animal-061220-023220.
10. Grishanin, A. (2014). Chromatin diminution in Copepoda (Crustacea): pattern, biological role and evolutionary aspects. Comp Cytogenet *8*, 1-10. 10.3897/CompCytogen.v8i1.5913.
11. Chen, J., Birchler, J.A., and Houben, A. (2022). The non-Mendelian behavior of plant B chromosomes. Chromosome Res *30*, 229-239. 10.1007/s10577-022-09687-4.
12. Borodin, P., Chen, A., Forstmeier, W., Fouche, S., Malinovskaya, L., Pei, Y., Reifova, R., Ruiz-Ruano, F.J., Schlebusch, S.A., Sotelo-Munoz, M., et al. (2022). Mendelian nightmares: the germline-restricted chromosome of songbirds. Chromosome Res. 10.1007/s10577-022-09688-3.
13. Rzeszutek, I., Maurer-Alcala, X.X., and Nowacki, M. (2020). Programmed genome rearrangements in ciliates. Cell Mol Life Sci. 10.1007/s00018-020-03555-2.
14. Herbette, M., and Ross, L. (2023). Paternal genome elimination: patterns and mechanisms of drive and silencing. Curr Opin Genet Dev *81*, 102065. 10.1016/j.gde.2023.102065.
15. Hanlon, V.C.T., Cagan, A., and Eves-van den Akker, S. (2025). How and when organisms edit their own genomes. Nat Genet. 10.1038/s41588-025-02230-1.
16. Bendich, A.J., and Rogers, S.O. (2025). The biological and evolutionary consequences of competition between DNA sequences that benefit the cell and DNA sequences that benefit themselves. Nucleic Acids Res *53*. 10.1093/nar/gkaf589.
17. Betermier, M., Klobutcher, L.A., and Orias, E. (2023). Programmed chromosome fragmentation in ciliated protozoa: multiple means to chromosome ends. Microbiol Mol Biol Rev, e0018422. 10.1128/mmbr.00184-22.
18. Simmons, J.R., Estrem, B., Zagoskin, M.V., Oldridge, R., Zadegan, S.B., and Wang, J. (2024). Chromosome fusion and programmed DNA elimination shape karyotypes of nematodes. Curr Biol *34*, 2147-2161 e2145. 10.1016/j.cub.2024.04.022.

19. Wang, J., Veronezi, G.M.B., Kang, Y., Zagoskin, M., O'Toole, E.T., and Davis, R.E. (2020). Comprehensive Chromosome End Remodeling during Programmed DNA Elimination. Curr Biol *30*, 3397–3413. 10.1016/j.cub.2020.06.058.
20. Wang, J., Gao, S., Mostovoy, Y., Kang, Y., Zagoskin, M., Sun, Y., Zhang, B., White, L.K., Easton, A., Nutman, T.B., et al. (2017). Comparative genome analysis of programmed DNA elimination in nematodes. Genome Res *27*, 2001-2014. 10.1101/gr.225730.117.
21. Zagoskin, M., Kang, Y., Davis, R.E., and Wang, J. (2025). Argonautes and small RNAs associated with nematode programmed DNA elimination. In bioRxiv.
22. Maharjan, P., Estrem, B., and Wang, J. (2025). R-loops are enriched at chromosome arms and associated with single-nucleotide polymorphisms in nematode Ascaris. In Preparation.
23. Dekker, J., and Mirny, L.A. (2024). The chromosome folding problem and how cells solve it. Cell *187*, 6424-6450. 10.1016/j.cell.2024.10.026.
24. McCord, R.P., Kaplan, N., and Giorgetti, L. (2020). Chromosome Conformation Capture and Beyond: Toward an Integrative View of Chromosome Structure and Function. Molecular cell *77*, 688-708. 10.1016/j.molcel.2019.12.021.
25. Zhang, Y., McCord, R.P., Ho, Y.J., Lajoie, B.R., Hildebrand, D.G., Simon, A.C., Becker, M.S., Alt, F.W., and Dekker, J. (2012). Spatial organization of the mouse genome and its role in recurrent chromosomal translocations. Cell *148*, 908-921. 10.1016/j.cell.2012.02.002.
26. Hu, J., Zhang, Y., Zhao, L., Frock, R.L., Du, Z., Meyers, R.M., Meng, F.L., Schatz, D.G., and Alt, F.W. (2015). Chromosomal Loop Domains Direct the Recombination of Antigen Receptor Genes. Cell *163*, 947-959. 10.1016/j.cell.2015.10.016.
27. Gassler, J., Brandao, H.B., Imakaev, M., Flyamer, I.M., Ladstatter, S., Bickmore, W.A., Peters, J.M., Mirny, L.A., and Tachibana, K. (2017). A mechanism of cohesin-dependent loop extrusion organizes zygotic genome architecture. Embo j *36*, 3600-3618. 10.15252/embj.201798083.
28. Kaaij, L.J.T., van der Weide, R.H., Ketting, R.F., and de Wit, E. (2018). Systemic Loss and Gain of Chromatin Architecture throughout Zebrafish Development. Cell reports *24*, 1-10 e14. 10.1016/j.celrep.2018.06.003.
29. Giorgetti, L., Lajoie, B.R., Carter, A.C., Attia, M., Zhan, Y., Xu, J., Chen, C.J., Kaplan, N., Chang, H.Y., Heard, E., and Dekker, J. (2016). Structural organization of the inactive X chromosome in the mouse. Nature *535*, 575-579. 10.1038/nature18589.
30. Minajigi, A., Froberg, J., Wei, C., Sunwoo, H., Kesner, B., Colognori, D., Lessing, D., Payer, B., Boukhali, M., Haas, W., and Lee, J.T. (2015). A comprehensive Xist interactome reveals cohesin repulsion and an RNA-directed chromosome conformation. Science (New York, N.Y.) *349*. 10.1126/science.aab2276.
31. Crane, E., Bian, Q., McCord, R.P., Lajoie, B.R., Wheeler, B.S., Ralston, E.J., Uzawa, S., Dekker, J., and Meyer, B.J. (2015). Condensin-driven remodelling of X chromosome topology during dosage compensation. Nature *523*, 240-244. 10.1038/nature14450.
32. Rabuffo, C., Schmidt, M.R., Yadav, P., Tong, P., Carloni, R., Barcons-Simon, A., Cosentino, R.O., Krebs, S., Matthews, K.R., Allshire, R.C., and Siegel, T.N. (2024). Inter-chromosomal transcription hubs shape the 3D genome architecture of African trypanosomes. Nat Commun *15*, 10716. 10.1038/s41467-024-55285-9.
33. Muller, L.S.M., Cosentino, R.O., Forstner, K.U., Guizetti, J., Wedel, C., Kaplan, N., Janzen, C.J., Arampatzi, P., Vogel, J., Steinbiss, S., et al. (2018). Genome organization and DNA accessibility control antigenic variation in trypanosomes. Nature *563*, 121-125. 10.1038/s41586-018-0619-8.

34. Bonev, B., Mendelson Cohen, N., Szabo, Q., Fritsch, L., Papadopoulos, G.L., Lubling, Y., Xu, X., Lv, X., Hugnot, J.P., Tanay, A., and Cavalli, G. (2017). Multiscale 3D Genome Rewiring during Mouse Neural Development. Cell *171*, 557-572 e524. 10.1016/j.cell.2017.09.043.
35. Rajarajan, P., Borrman, T., Liao, W., Schrode, N., Flaherty, E., Casino, C., Powell, S., Yashaswini, C., LaMarca, E.A., Kassim, B., et al. (2018). Neuron-specific signatures in the chromosomal connectome associated with schizophrenia risk. Science (New York, N.Y.) *362*. 10.1126/science.aat4311.
36. Estrem, B., Davis, R.E., and Wang, J. (2024). End resection and telomere healing of DNA double-strand breaks during nematode programmed DNA elimination. Nucleic Acids Res *52*, 8913-8929. 10.1093/nar/gkae579.
37. Strom, A.R., Emelyanov, A.V., Mir, M., Fyodorov, D.V., Darzacq, X., and Karpen, G.H. (2017). Phase separation drives heterochromatin domain formation. Nature *547*, 241-245. 10.1038/nature22989.
38. Feric, M., and Misteli, T. (2021). Phase separation in genome organization across evolution. Trends Cell Biol *31*, 671-685. 10.1016/j.tcb.2021.03.001.
39. Goloborodko, A., Imakaev, M.V., Marko, J.F., and Mirny, L. (2016). Compaction and segregation of sister chromatids via active loop extrusion. Elife *5*. 10.7554/eLife.14864.
40. Zheng, H., and Xie, W. (2019). The role of 3D genome organization in development and cell differentiation. Nature reviews. Molecular cell biology *20*, 535-550. 10.1038/s41580-019-0132-4.
41. Li, H., Playter, C., Das, P., and McCord, R.P. (2024). Chromosome compartmentalization: causes, changes, consequences, and conundrums. Trends Cell Biol *34*, 707-727. 10.1016/j.tcb.2024.01.009.
42. Lajoie, B.R., Dekker, J., and Kaplan, N. (2015). The Hitchhiker's guide to Hi-C analysis: practical guidelines. Methods (San Diego, Calif.) *72*, 65-75. 10.1016/j.ymeth.2014.10.031.
43. Sawh, A.N., Shafer, M.E.R., Su, J.H., Zhuang, X., Wang, S., and Mango, S.E. (2020). Lamina-Dependent Stretching and Unconventional Chromosome Compartments in Early C. elegans Embryos. Molecular cell *78*, 96-111 e116. 10.1016/j.molcel.2020.02.006.
44. Jash, E., and Csankovszki, G. (2024). Chromatin Organization during C. elegans Early Development. DNA (Basel) *4*, 64-83. 10.3390/dna4010004.
45. Wang, J., and Davis, R.E. (2020). Ascaris. Curr Biol *30*, R423-R425. 10.1016/j.cub.2020.02.064.
46. Sabari, B.R., Dall'Agnese, A., and Young, R.A. (2020). Biomolecular Condensates in the Nucleus. Trends Biochem Sci *45*, 961-977. 10.1016/j.tibs.2020.06.007.
47. Shin, Y., and Brangwynne, C.P. (2017). Liquid phase condensation in cell physiology and disease. Science (New York, N.Y.) *357*. 10.1126/science.aaf4382.
48. Hyman, A.A., Weber, C.A., and Julicher, F. (2014). Liquid-liquid phase separation in biology. Annu Rev Cell Dev Biol *30*, 39-58. 10.1146/annurev-cellbio-100913-013325.
49. Fujishiro, S., Sasai, M., and Maeshima, K. (2025). Chromatin domains in the cell: Phase separation and condensation. Current opinion in structural biology *91*, 103006. 10.1016/j.sbi.2025.103006.
50. Pulupa, J., McArthur, N.G., Stathi, O., Wang, M., Zazhytska, M., Pirozzolo, I.D., Nayar, A., Shapiro, L., and Lomvardas, S. (2025). Solid phase transitions as a solution to the genome folding paradox. Nature *643*, 820-829. 10.1038/s41586-025-09043-6.
51. Spegg, V., Panagopoulos, A., Stout, M., Krishnan, A., Reginato, G., Imhof, R., Roschitzki, B., Cejka, P., and Altmeyer, M. (2023). Phase separation properties of RPA combine high-affinity ssDNA binding with dynamic condensate functions at telomeres. Nature structural & molecular biology *30*, 451-462. 10.1038/s41594-023-00932-w.

52. Soranno, A., Incicco, J.J., De Bona, P., Tomko, E.J., Galburt, E.A., Holehouse, A.S., and Galletto, R. (2022). Shelterin Components Modulate Nucleic Acids Condensation and Phase Separation in the Context of Telomeric DNA. J Mol Biol *434*, 167685. 10.1016/j.jmb.2022.167685.
53. Jack, A., Kim, Y., Strom, A.R., Lee, D.S.W., Williams, B., Schaub, J.M., Kellogg, E.H., Finkelstein, I.J., Ferro, L.S., Yildiz, A., and Brangwynne, C.P. (2022). Compartmentalization of telomeres through DNA-scaffolded phase separation. Dev Cell *57*, 277-290 e279. 10.1016/j.devcel.2021.12.017.
54. Giudice, J., and Jiang, H. (2024). Splicing regulation through biomolecular condensates and membraneless organelles. Nature reviews. Molecular cell biology *25*, 683-700. 10.1038/s41580-024-00739-7.
55. MacQueen, A.J., Phillips, C.M., Bhalla, N., Weiser, P., Villeneuve, A.M., and Dernburg, A.F. (2005). Chromosome sites play dual roles to establish homologous synapsis during meiosis in C. elegans. Cell *123*, 1037-1050. 10.1016/j.cell.2005.09.034.
56. Phillips, C.M., and Dernburg, A.F. (2006). A family of zinc-finger proteins is required for chromosome-specific pairing and synapsis during meiosis in C. elegans. Dev Cell *11*, 817-829. 10.1016/j.devcel.2006.09.020.
57. Niedermaier, J., and Moritz, K.B. (2000). Organization and dynamics of satellite and telomere DNAs in Ascaris: implications for formation and programmed breakdown of compound chromosomes. Chromosoma *109*, 439-452.
58. Chiolo, I., Altmeyer, M., Legube, G., and Mekhail, K. (2025). Nuclear and genome dynamics underlying DNA double-strand break repair. Nature reviews. Molecular cell biology *26*, 538-557. 10.1038/s41580-025-00828-1.
59. Sanders, J.T., Freeman, T.F., Xu, Y., Golloshi, R., Stallard, M.A., Hill, A.M., San Martin, R., Balajee, A.S., and McCord, R.P. (2020). Radiation-induced DNA damage and repair effects on 3D genome organization. Nat Commun *11*, 6178. 10.1038/s41467-020-20047-w.
60. Arnould, C., Rocher, V., Saur, F., Bader, A.S., Muzzopappa, F., Collins, S., Lesage, E., Le Bozec, B., Puget, N., Clouaire, T., et al. (2023). Chromatin compartmentalization regulates the response to DNA damage. Nature *623*, 183-192. 10.1038/s41586-023-06635-y.
61. Zagelbaum, J., Schooley, A., Zhao, J., Schrank, B.R., Callen, E., Zha, S., Gottesman, M.E., Nussenzweig, A., Rabadan, R., Dekker, J., and Gautier, J. (2023). Multiscale reorganization of the genome following DNA damage facilitates chromosome translocations via nuclear actin polymerization. Nature structural & molecular biology *30*, 99-106. 10.1038/s41594-022-00893-6.
62. Muller, F., Wicky, C., Spicher, A., and Tobler, H. (1991). New telomere formation after developmentally regulated chromosomal breakage during the process of chromatin diminution in Ascaris lumbricoides. Cell *67*, 815-822.
63. Bian, Q., Anderson, E.C., Yang, Q., and Meyer, B.J. (2020). Histone H3K9 methylation promotes formation of genome compartments in Caenorhabditis elegans via chromosome compaction and perinuclear anchoring. Proc Natl Acad Sci U S A *117*, 11459-11470. 10.1073/pnas.2002068117.
64. Kim, J., Jimenez, D.S., Ragipani, B., Zhang, B., Street, L.A., Kramer, M., Albritton, S.E., Winterkorn, L.H., Morao, A.K., and Ercan, S. (2022). Condensin DC loads and spreads from recruitment sites to create loop-anchored TADs in C. elegans. Elife *11*. 10.7554/eLife.68745.
65. Kim, J., Wang, H., and Ercan, S. (2025). Cohesin organizes 3D DNA contacts surrounding active enhancers in C. elegans. Genome research *35*, 1108-1123. 10.1101/gr.279365.124.

66. Das, M., Semple, J.I., Haemmerli, A., Volodkina, V., Scotton, J., Gitchev, T., Annan, A., Campos, J., Statzer, C., Dakhovnik, A., et al. (2024). Condensin I folds the Caenorhabditis elegans genome. Nat Genet *56*, 1737-1749. 10.1038/s41588-024-01832-5.
67. Sawh, A.N., and Mango, S.E. (2022). Chromosome organization in 4D: insights from C. elegans development. Current opinion in genetics & development *75*, 101939. 10.1016/j.gde.2022.101939.
68. Gerstein, M.B., Lu, Z.J., Van Nostrand, E.L., Cheng, C., Arshinoff, B.I., Liu, T., Yip, K.Y., Robilotto, R., Rechtsteiner, A., Ikegami, K., et al. (2010). Integrative analysis of the Caenorhabditis elegans genome by the modENCODE project. Science (New York, N.Y.) *330*, 1775-1787. 10.1126/science.1196914.
69. Gonzalez de la Rosa, P.M., Thomson, M., Trivedi, U., Tracey, A., Tandonnet, S., and Blaxter, M. (2021). A telomere-to-telomere assembly of Oscheius tipulae and the evolution of rhabditid nematode chromosomes. G3 (Bethesda) *11*. 10.1093/g3journal/jkaa020.
70. Tandonnet, S., Koutsovoulos, G.D., Adams, S., Cloarec, D., Parihar, M., Blaxter, M.L., and Pires-daSilva, A. (2019). Chromosome-Wide Evolution and Sex Determination in the Three-Sexed Nematode Auanema rhodensis. G3 (Bethesda) *9*, 1211-1230. 10.1534/g3.119.0011.
71. Yoshida, K., Rodelsperger, C., Roseler, W., Riebesell, M., Sun, S., Kikuchi, T., and Sommer, R.J. (2023). Chromosome fusions repatterned recombination rate and facilitated reproductive isolation during Pristionchus nematode speciation. Nature ecology & evolution *7*, 424-439. 10.1038/s41559-022-01980-z.
72. Dockendorff, T.C., Estrem, B., Reed, J., Simmons, J.R., Zadegan, S.B., Zagoskin, M.V., Terta, V., Villalobos, E., Seaberry, E.M., and Wang, J. (2022). The nematode Oscheius tipulae as a genetic model for programmed DNA elimination. Curr Biol *32*, 5083-5098 e5086. 10.1016/j.cub.2022.10.043.
73. Villano, D.J., Prahlad, M., Singhal, A., Sanbonmatsu, K.Y., and Landweber, L.F. (2025). Widespread 3D genome reorganization precedes programmed DNA rearrangement in Oxytricha trifallax. bioRxiv. 10.1101/2024.12.31.630814.
74. Bracht, J.R., Fang, W., Goldman, A.D., Dolzhenko, E., Stein, E.M., and Landweber, L.F. (2013). Genomes on the edge: programmed genome instability in ciliates. Cell *152*, 406-416. 10.1016/j.cell.2013.01.005.
75. Noto, T., and Mochizuki, K. (2017). Whats, hows and whys of programmed DNA elimination in Tetrahymena. Open Biol *7*. 10.1098/rsob.170172.
76. Wang, J., Garrey, J., and Davis, R.E. (2014). Transcription in pronuclei and one- to four-cell embryos drives early development in a nematode. Current biology : CB *24*, 124-133. 10.1016/j.cub.2013.11.045.
77. Kang, Y., Wang, J., Neff, A., Kratzer, S., Kimura, H., and Davis, R.E. (2016). Differential Chromosomal Localization of Centromeric Histone CENP-A Contributes to Nematode Programmed DNA Elimination. Cell Rep. 10.1016/j.celrep.2016.07.079.
78. Altschul, S.F., Madden, T.L., Schaffer, A.A., Zhang, J., Zhang, Z., Miller, W., and Lipman, D.J. (1997). Gapped BLAST and PSI-BLAST: a new generation of protein database search programs. Nucleic Acids Res *25*, 3389-3402. 10.1093/nar/25.17.3389.
79. Langmead, B., and Salzberg, S.L. (2012). Fast gapped-read alignment with Bowtie 2. Nat Methods *9*, 357-359. 10.1038/nmeth.1923.
80. Servant, N., Varoquaux, N., Lajoie, B.R., Viara, E., Chen, C.J., Vert, J.P., Heard, E., Dekker, J., and Barillot, E. (2015). HiC-Pro: an optimized and flexible pipeline for Hi-C data processing. Genome biology *16*, 259. 10.1186/s13059-015-0831-x.
81. Lieberman-Aiden, E., van Berkum, N.L., Williams, L., Imakaev, M., Ragoczy, T., Telling, A., Amit, I., Lajoie, B.R., Sabo, P.J., Dorschner, M.O., et al. (2009). Comprehensive mapping of

long-range interactions reveals folding principles of the human genome. Science (New York, N.Y.) *326*, 289-293. 10.1126/science.1181369.

82. Kruse, K., Hug, C.B., and Vaquerizas, J.M. (2020). FAN-C: a feature-rich framework for the analysis and visualisation of chromosome conformation capture data. Genome biology *21*, 303. 10.1186/s13059-020-02215-9.

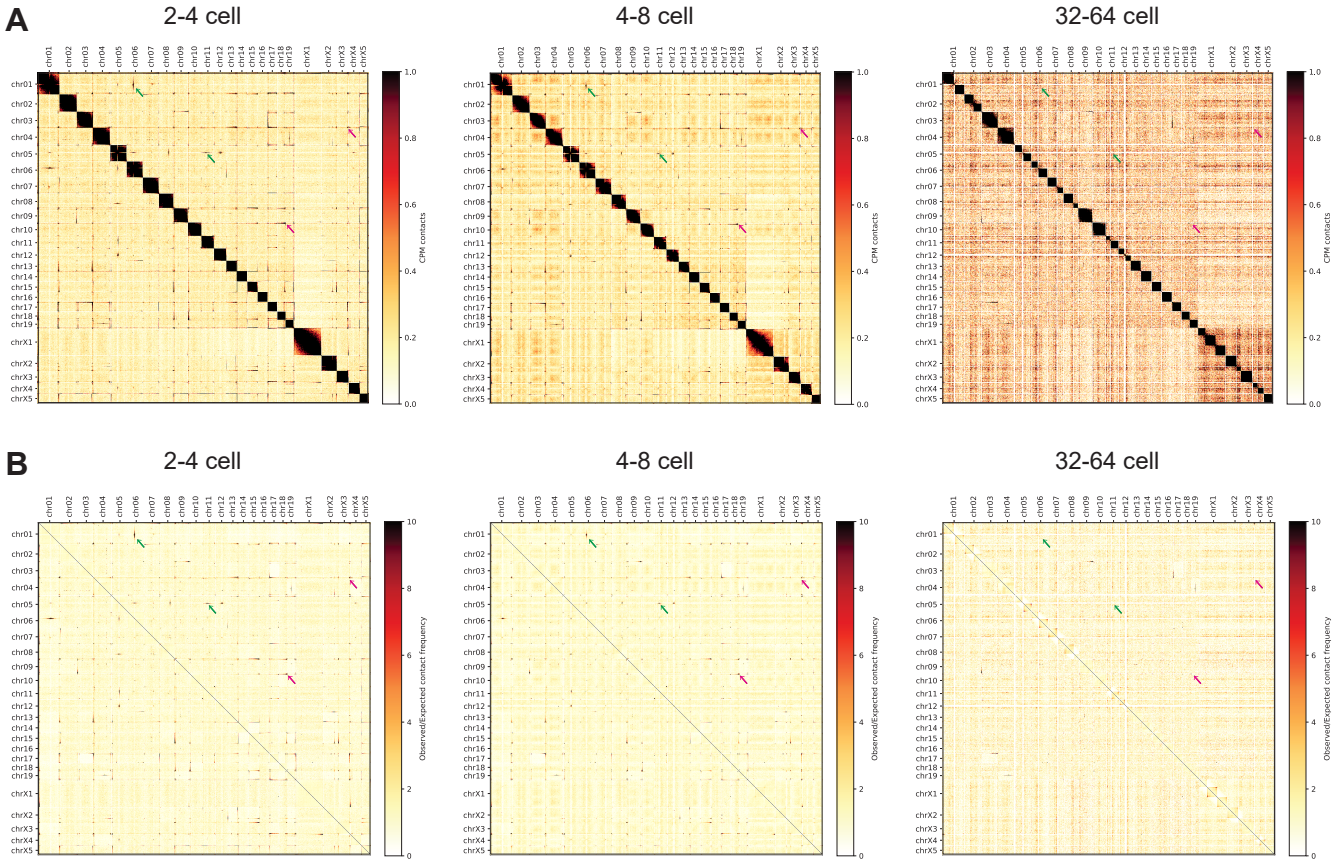
A
2-4 cell
4-8 cell
32-64 cell
CPM contacts
B
2-4 cell
4-8 cell
32-64 cell
Observed/Expected contact frequency

Figure 1

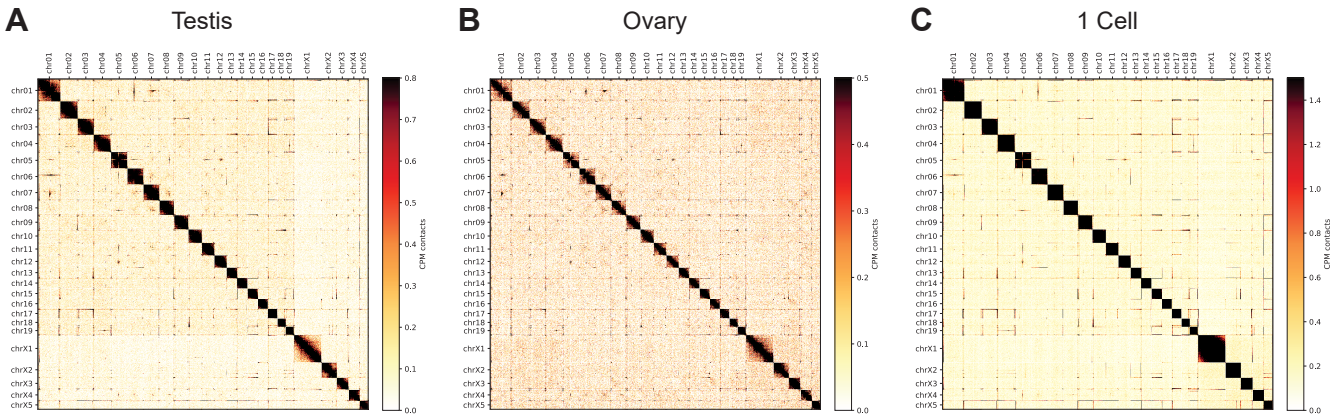

Figure 2

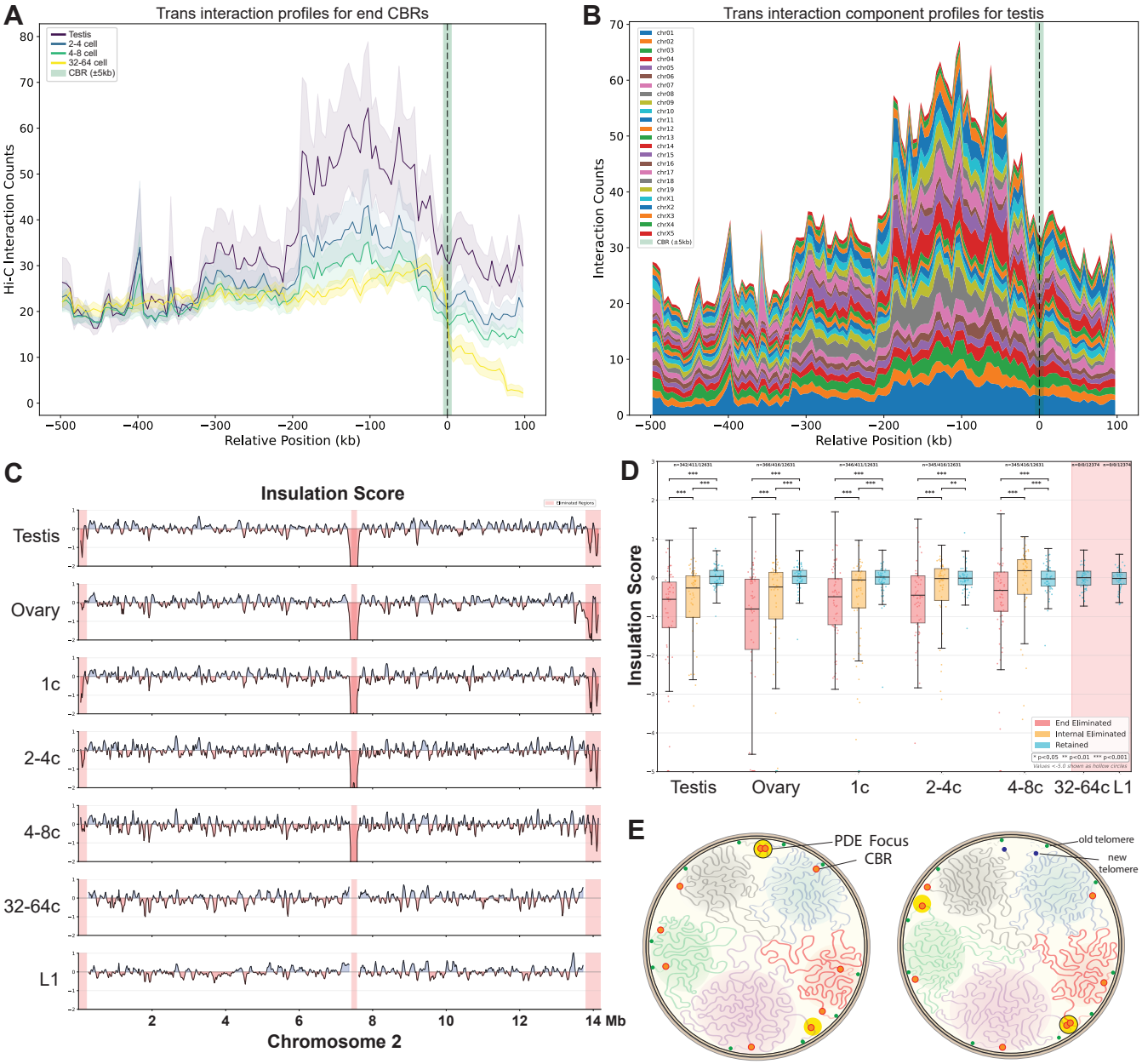
A
Trans interaction profiles for end CBRs
Testis
2-4 cell
4-8 cell
32-64 cell
CBR (±5kb)
Hi-C Interaction Counts
Relative Position (kb)
B
Trans interaction component profiles for testis
Interaction Counts
Relative Position (kb)
C
Insulation Score
Testis
Ovary
1c
2-4c
4-8c
32-64c
L1
Chromosome 2
D
Insulation Score
End Eliminated
Internal Eliminated
Retained
Testis
Ovary
1c
2-4c
4-8c
32-64c
L1
E
PDE Focus
CBR
old telomere
new telomere

Figure 3

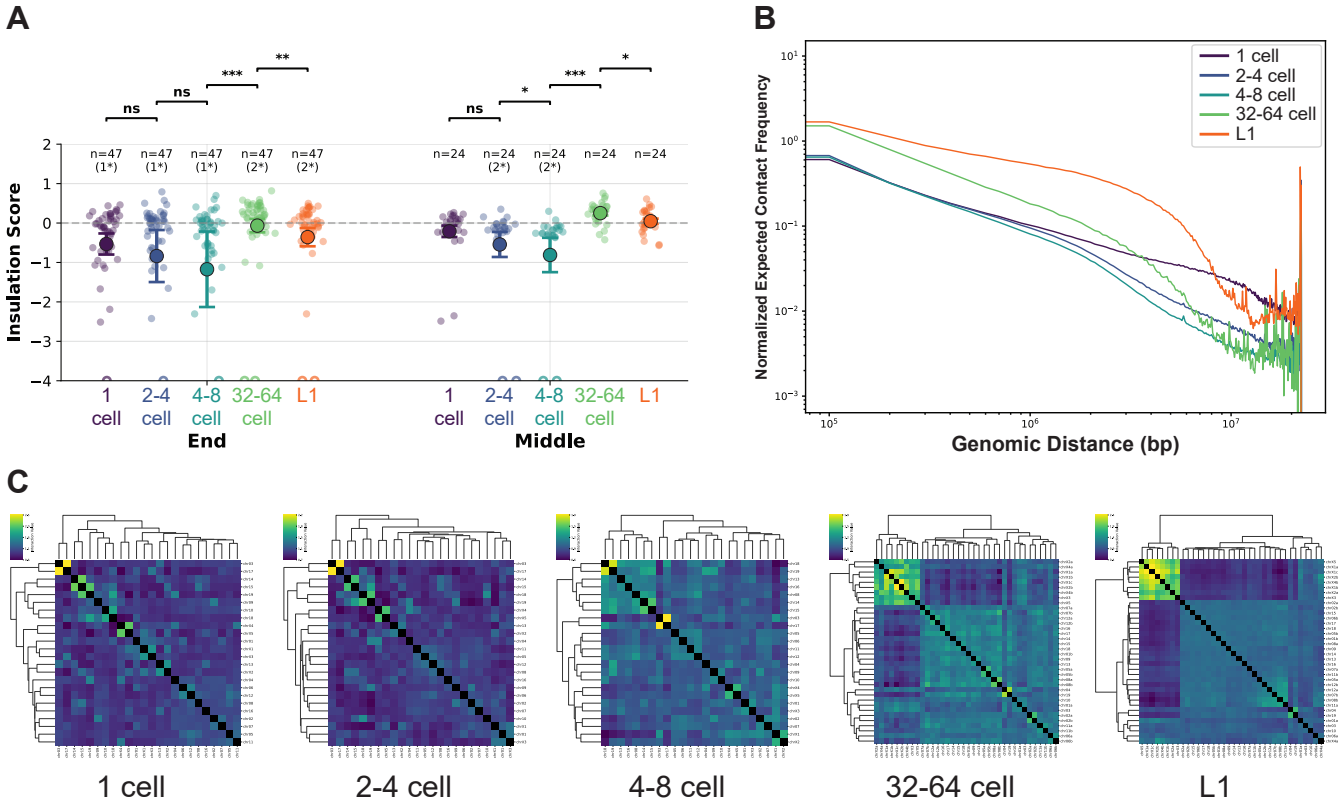
A
B
C
Insulation Score
ns
ns
***
**
ns
*
***
*
n=47 (1*)
n=47 (1*)
n=47 (1*)
n=47 (2*)
n=47 (2*)
n=24
n=24 (2*)
n=24 (2*)
n=24
n=24
1 cell
2-4 cell
4-8 cell
32-64 cell
L1
End
Middle
Normalized Expected Contact Frequency
Genomic Distance (bp)
1 cell
2-4 cell
4-8 cell
32-64 cell
L1

Figure 4

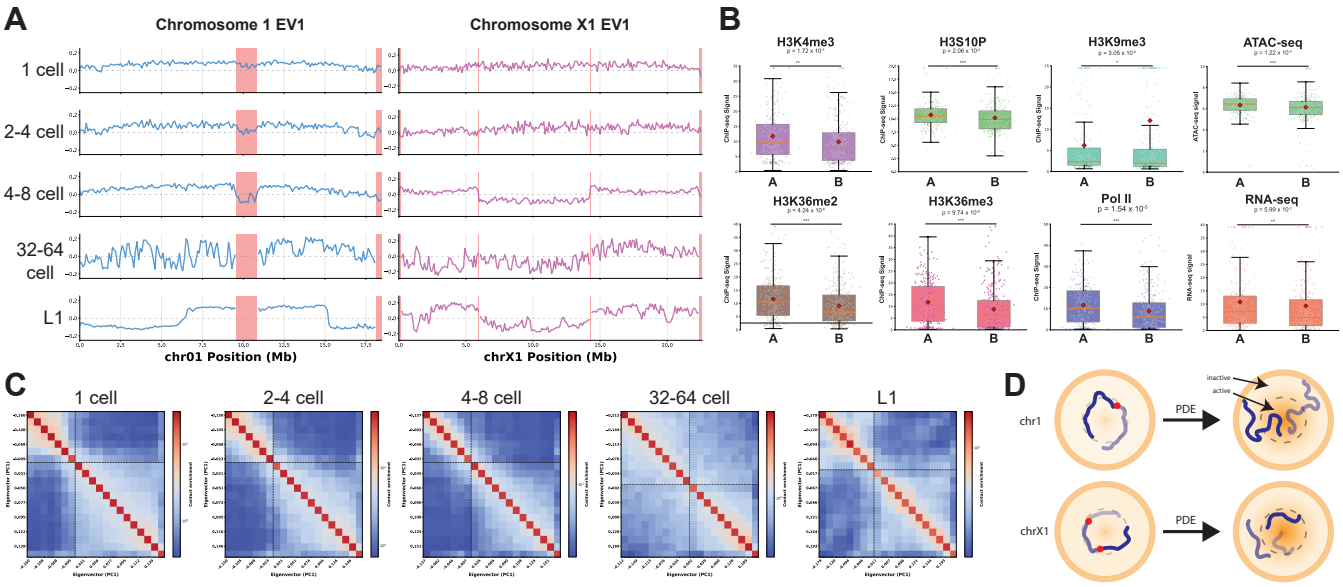
A
Chromosome 1 EV1
Chromosome X1 EV1
1 cell
2-4 cell
4-8 cell
32-64 cell
L1
chr01 Position (Mb)
chrX1 Position (Mb)
B
H3K4me3
H3S10P
H3K9me3
ATAC-seq
H3K36me2
H3K36me3
Pol II
RNA-seq
A
B
C
1 cell
2-4 cell
4-8 cell
32-64 cell
L1
D
chr1
chrX1
PDE
PDE
inactive
active

Figure 5

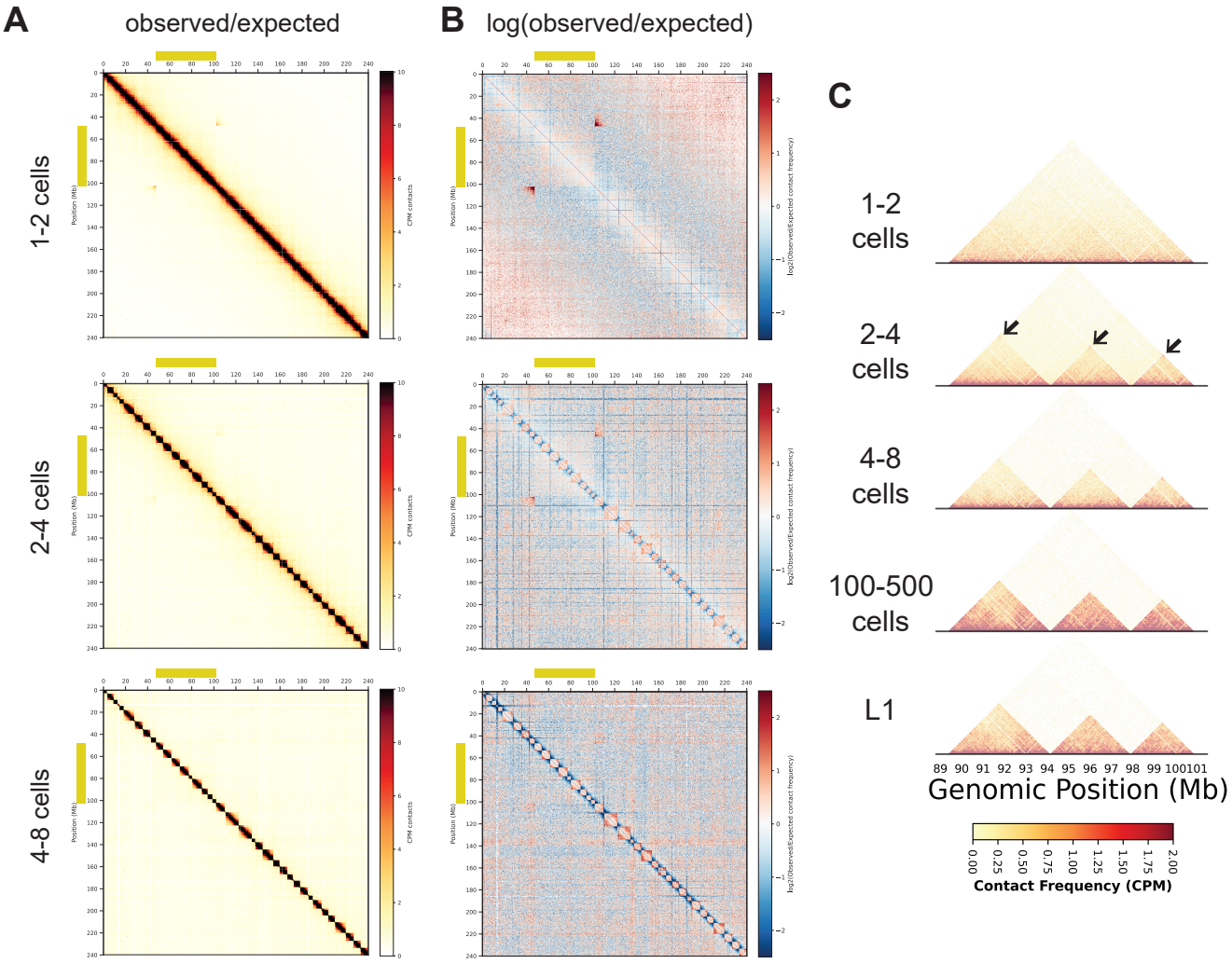
A
observed/expected
B
log(observed/expected)
C
1-2 cells
2-4 cells
4-8 cells
100-500 cells
L1
Genomic Position (Mb)
Contact Frequency (CPM)

Figure 6

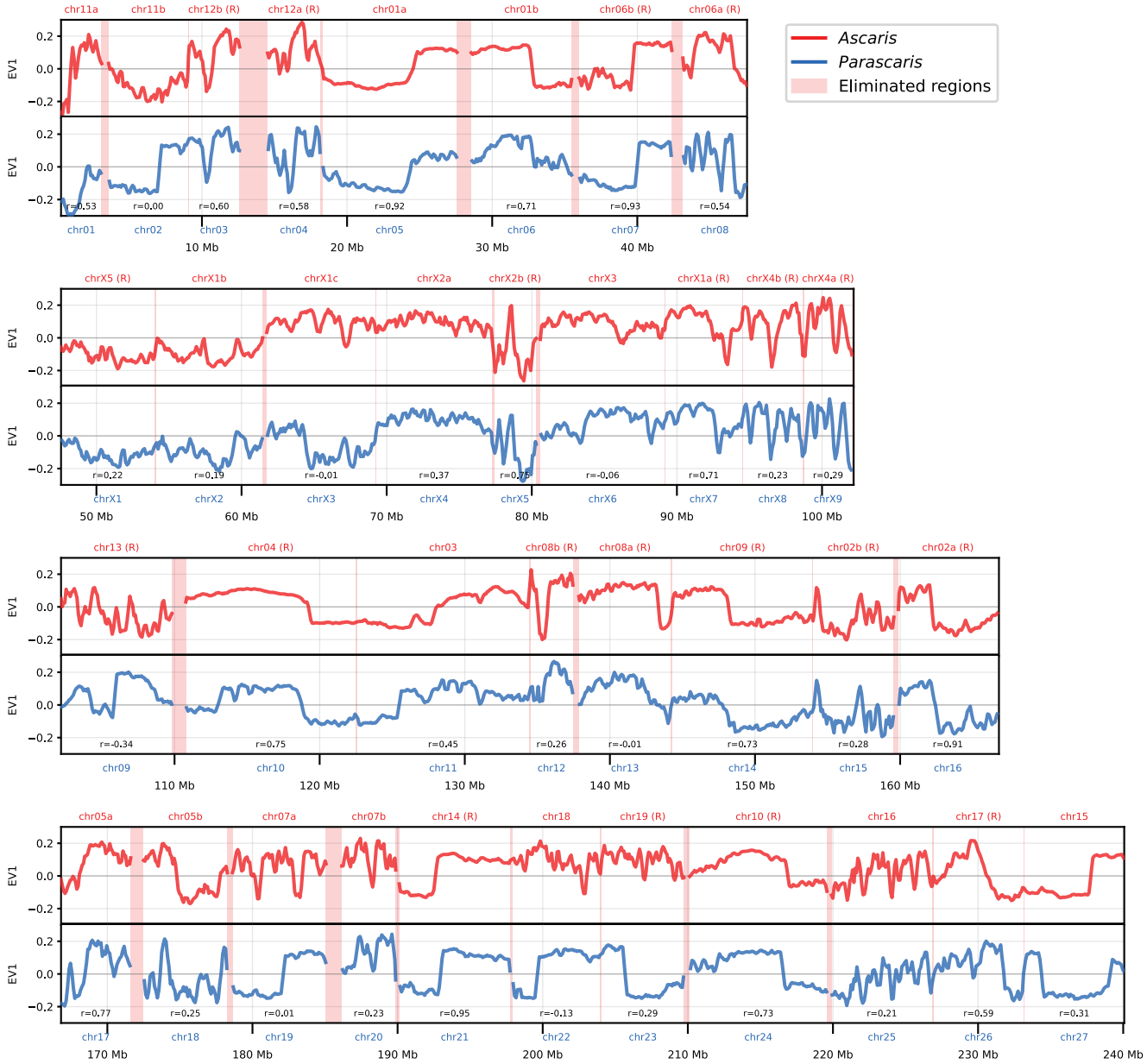
Ascaris
Parascaris
Eliminated regions
EV1
chr11a
chr11b
chr12b (R)
chr12a (R)
chr01a
chr01b
chr06b (R)
chr06a (R)
r=0.53
r=0.00
r=0.60
r=0.58
r=0.92
r=0.71
r=0.93
r=0.54
chr01
chr02
chr03
chr04
chr05
chr06
chr07
chr08
10 Mb
20 Mb
30 Mb
40 Mb
chrX5 (R)
chrX1b
chrX1c
chrX2a
chrX2b (R)
chrX3
chrX1a (R)
chrX4b (R)
chrX4a (R)
r=0.22
r=0.19
r=-0.01
r=0.37
r=0.75
r=-0.06
r=0.71
r=0.23
r=0.29
chrX1
chrX2
chrX3
chrX4
chrX5
chrX6
chrX7
chrX8
chrX9
50 Mb
60 Mb
70 Mb
80 Mb
90 Mb
100 Mb
chr13 (R)
chr04 (R)
chr03
chr08b (R)
chr08a (R)
chr09 (R)
chr02b (R)
chr02a (R)
r=-0.34
r=0.75
r=0.45
r=0.26
r=-0.01
r=0.73
r=0.28
r=0.91
chr09
chr10
chr11
chr12
chr13
chr14
chr15
chr16
110 Mb
120 Mb
130 Mb
140 Mb
150 Mb
160 Mb
chr05a
chr05b
chr07a
chr07b
chr14 (R)
chr18
chr19 (R)
chr10 (R)
chr16
chr17 (R)
chr15
r=0.77
r=0.25
r=0.01
r=0.23
r=0.95
r=-0.13
r=0.29
r=0.73
r=0.21
r=0.59
r=0.31
chr17
chr18
chr19
chr20
chr21
chr22
chr23
chr24
chr25
chr26
chr27
170 Mb
180 Mb
190 Mb
200 Mb
210 Mb
220 Mb
230 Mb
240 Mb

Figure 7